

Disorders of the Nervous System

# Glycolytic System in Axons Supplement Decreased ATP Levels after Axotomy of the Peripheral Nerve

Tomofumi Takenaka,<sup>1,2</sup> Yuichiro Ohnishi,<sup>2,3</sup> Masamichi Yamamoto,<sup>2</sup> Daiki Setoyama,<sup>4</sup> and Haruhiko Kishima<sup>1</sup>

<https://doi.org/10.1523/ENEURO.0353-22.2023>

<sup>1</sup>Department of neurosurgery, Graduate School of Medicine, Osaka University, Osaka, 565-0871, Japan, <sup>2</sup>Department of Research Promotion and Management, National Cerebral and Cardiovascular Center, Osaka, 564-8565, Japan, <sup>3</sup>Department of Neurosurgery, Osaka Gyoumeikan Hospital, Osaka, 554-0012, Japan, and <sup>4</sup>Department of Clinical Chemistry and Laboratory Medicine, Graduate School of Medical Sciences, Kyushu University, Fukuoka, 812-8582, Japan

## Abstract

Wallerian degeneration (WD) occurs in the early stages of numerous neurologic disorders, and clarifying WD pathology is crucial for the advancement of neurologic therapies. ATP is acknowledged as one of the key pathologic substances in WD. The ATP-related pathologic pathways that regulate WD have been defined. The elevation of ATP levels in axon contributes to delay WD and protects axons. However, ATP is necessary for the active processes to proceed WD, given that WD is stringently managed by auto-destruction programs. But little is known about the bioenergetics during WD. In this study, we made sciatic nerve transection models for *GO-ATeam2* knock-in rats and mice. We presented the spatiotemporal ATP distribution in the injured axons with *in vivo* ATP imaging systems, and investigated the metabolic source of ATP in the distal nerve stump. A gradual decrease in ATP levels was observed before the progression of WD. In addition, the glycolytic system and monocarboxylate transporters (MCTs) were activated in Schwann cells following axotomy. Interestingly, in axons, we found the activation of glycolytic system and the inactivation of the tricarboxylic acid (TCA) cycle. Glycolytic inhibitors, 2-deoxyglucose (2-DG) and MCT inhibitors, α-cyano-4-hydroxycinnamic acid (4-CIN) decreased ATP and enhanced WD progression, whereas mitochondrial pyruvate carrier (MPC) inhibitors (MSDC-0160) did not change. Finally, ethyl pyruvate (EP) increased ATP levels and delayed WD. Together, our findings suggest that glycolytic system, both in Schwann cells and axons, is the main source of maintaining ATP levels in the distal nerve stump.

**Key words:** ATP; glycolytic system; *in vivo* imaging; mitochondria; Wallerian degeneration

## Significance Statement

Wallerian degeneration (WD) after axotomy is associated with decreasing ATP levels. To maintain ATP levels, Schwann cells activate the glycolytic systems and produce monocarboxylate, which is transported to axons via monocarboxylate transporters (MCTs). Axons also activate the glycolysis system to obtain ATP, and inactivate tricarboxylic acid (TCA) cycle because of mitochondrial degeneration. The glycolysis with MCT-induced monocarboxylate transport contributes to the ATP production in degenerative axons.

## Introduction

Wallerian degeneration (WD) refers to programmed axon degeneration, which is classically defined as the pathology of the distal nerve stump following injury (Waller,

1851). Recent studies revealed that key pathologic features of WD occur in chronic neurologic disorders as well as acute traumatic injuries (J.T. Wang et al., 2012; Conforti et al., 2014; Coleman and Höke, 2020), to the

Received August 30, 2022; accepted February 25, 2023; First published March 9, 2023.

The authors declare no competing financial interests.

Author contributions: T.T. and Y.O. designed research; T.T., Y.O., M.Y., and D.S. performed research; T.T. analyzed data; T.T., Y.O., and H.K. wrote the paper.

mammalian CNS or peripheral nervous system (PNS; Vargas and Barres, 2007; Beirowski et al., 2010). Therefore, elucidating the pathology of WD is important in developing therapies that can prevent or delay axonal degeneration and loss of function in various axonopathy-driven disorders, such as peripheral and central nerve injury, cerebral infarction, and neurologic disorders.

ATP is one of the key pathologic substances in WD. The elevation of ATP levels in axons delays WD (J. Wang et al., 2005; Yang et al., 2015), and supports axon regeneration (Han et al., 2016; Zhou et al., 2016). Previous studies have been reported the ATP-related pathologic pathways involved in WD. First, ATP is used in the salvage pathway. Nicotinamide mononucleotide (NMN) and ATP are catalyzed by nicotinamide mononucleotide adenylyl transferase 2 (NMNAT2) to form nicotinamide adenine dinucleotide (NAD<sup>+</sup>; Lau et al., 2009; Gilley and Coleman, 2010). NAD<sup>+</sup> is a critical factor in maintaining the distal nerve stump ATP levels during WD (Araki et al., 2004; Gerdtts et al., 2015). Second, ATP is required for WD progression (Conforti et al., 2014). One of the main proposed mechanisms is axonal autophagy (Nixon, 2013), which is thought to contribute to local ATP production that drives WD (Wakatsuki et al., 2017). However, from a bioenergetics perspective, the specifics of these salvage pathways and auto-destruction programs in WD remains unknown (J.T. Wang et al., 2012; Yang et al., 2015; Gerdtts et al., 2016; Babetto et al., 2020; Coleman and Höke, 2020). Especially, the spatiotemporal distribution and the metabolic source of ATP during WD remains elusive.

Recent studies suggested that activating the glycolytic system in Schwann cells and monocarboxylate supplementation to axons via monocarboxylate transporters (MCTs) is important for maintaining ATP levels, delaying WD, and promoting axon regeneration (Babetto et al., 2020; Li et al., 2020; Trimarco and Taveggia, 2020). The metabolic interaction between Schwann cells and axons is important for neuronal survival (Bouçanova and Chrast, 2020). However, mitochondria become dysfunctional in the early stages of WD (B. Wang et al., 2021), with dilated and disorganized cristae (J. Wang et al., 2011), and mitochondrial dysfunction would lead to reduced ATP production in the tricarboxylic acid (TCA) cycle (Pivovarova and Andrews, 2010); therefore, it is questionable whether

axonal mitochondria metabolize the transported monocarboxylates in degenerative axons. Furthermore, axons in the distal nerve stump are incapable of transporting mitochondria to the caudal side, which results in a dramatic decline in both anterograde and retrograde axonal transport 24 h after axotomy (Misgeld et al., 2007). Study results remain controversial and the ATP-generating metabolic pathways, using monocarboxylates, in injured axons remain undefined.

In this study, we investigated the spatiotemporal ATP levels in injured peripheral nerves by using *in vivo* ATP imaging systems (Nakano et al., 2011; Yamamoto et al., 2019; Ohnishi et al., 2021; Nakajima et al., 2022). In addition, we explored the metabolic source of ATP in degenerative axons using mass spectrometry, histologic analysis, and pharmacological intervention.

## Materials and Methods

### Animals

All procedures were performed in accordance with the guidelines of the Laboratory Animal Care and Use Committee of Osaka University, Japan (No. 29-025-015). *GO-ATeam2* knock-in mice and rats were generated by M.Y. Briefly, we employed a knock-in strategy targeting the *Rosa26* locus and the CAG promoter to regulate transcription, for generating both *GO-ATeam2* knock-in mice (Yamamoto et al., 2019) and rats (our unpublished observations). *GO-ATeam2* knock-in mice were generated by inducing targeting vectors into G4 ES cells through electroporation and breeding chimeric mice for at least five generations. *GO-ATeam2* knock-in rats were generated by CRISPR/Cas9-based genome editing system (Cong et al., 2013). Mice and rats were housed in cages of three animals at  $24 \pm 2^\circ\text{C}$  under a 12/12 h light/dark cycle (8 P.M. lights off, 8 A.M. lights on), and were allowed free access to fast water overnight. The cages were cleaned twice a week. *GO-ATeam2* knock-in rats (SD background, 300–450 g, four to six rats per group) were used to measure ATP levels by fluorescence microscopy and histologic evaluation. *GO-ATeam2* knock-in mice (ICR background, 35–45 g, three to six mice per group) were used to measure ATP levels using fluorescence microscopy or two-photon microscopy, histologic evaluation, mass spectrometry, and local administration of inhibitor or ethyl pyruvate (EP). In the earlier part of the experiment, we used rats, which are more suitable for modeling human disorders and easier to surgically manipulate (Adalbert et al., 2005). As the experiment proceeds, we used mice because the experiments involving two-photon microscopy were unsuitable for the body size of rats. Mixed sexes were used because previous studies showed no significant difference between the sexes and the rates of axon degeneration because of injury (Babetto et al., 2020). All animals were 7–12 weeks in age. We made the best effort to minimize the number of animals used.

### Sciatic nerve transection models

We created the same transection model for *GO-ATeam2* knock-in mice and rats as previously reported

This work was supported by the JSPS KAKENHI Grant Number JP 20K17967, the JSPS KAKENHI Grant Number 18H04085, and the AMED Grant Number JP20ek0610017.

Acknowledgments: We thank Tomoaki Mizuno and Eiji Oiki (Center for Medical Research and Education, Graduate School of Medicine, Osaka University) for their technical support in performing epon-embedded treatment of the sciatic nerve. We would like to thank the Nikon Imaging Center at Osaka University for technical support. We would also like to thank Editage for English language editing.

Correspondence should be addressed to Yuichiro Ohnishi at [ohnishisurg@gmail.com](mailto:ohnishisurg@gmail.com) or Haruhiko Kishima at [hkishima@nsurg.med.osaka-u.ac.jp](mailto:hkishima@nsurg.med.osaka-u.ac.jp).

<https://doi.org/10.1523/ENEURO.0353-22.2023>

Copyright © 2023 Takenaka et al.

This is an open-access article distributed under the terms of the Creative Commons Attribution 4.0 International license, which permits unrestricted use, distribution and reproduction in any medium provided that the original work is properly attributed.

(Savastano et al., 2014). Briefly, mice and rats were deeply anesthetized with 4% isoflurane and maintained with 2% isoflurane in air. The animal's body temperature was maintained at 36.0–37.0°C using a heating pad. A minimum skin incision was made 5 mm caudal and along the femur, and the right sciatic nerves were gently exposed and transected with micro scissors at the level of the sciatic notch. The wound was closed using surgical thread. During the target period, animals were killed by deep sedation after ATP imaging or harvesting of sciatic nerve lesions. Histologic evaluation (epifluorescence, confocal microscopy, electron microscopy) was performed 3 mm distal from the sectional end (Extended Data Figs. 1-1, 3-1). Distal sciatic nerve stumps (~7-mm continuous from the sectional end) were harvested for mass spectrometry. Separate individuals were used for ATP imaging, histologic evaluation, and mass spectrometry.

### ATP imaging

The *GO-ATeam2* probe expresses a fluorescence/Forster resonance energy transfer (FRET) pair as an ATP biosensor with orange fluorescent protein (OFP) and green fluorescent protein (GFP; Nakano et al., 2011). Specific binding of ATP to the  $\epsilon$  subunit of the *GO-ATeam2* probe causes a conformational change in the  $\epsilon$  subunit from the extended to the retracted form, increasing the FRET efficiency (Yagi, 2007). OFP and GFP were used as FRET donors and acceptors, respectively, and the OFP/GFP ratio was quantitatively calculated as the ATP levels in the cytoplasm. The obtained OFP/GFP ratio was applied to the following equation:  $\text{FRET ratio} = 1.52 \times [\text{ATP}]^{1.7} / ([\text{ATP}]^{1.7} + 2.22) + 0.44$ , and then, ATP concentration was calculated. The coefficients were carefully determined based on two methods (Yamamoto et al., 2019). First, mouse embryonic fibroblasts were obtained from *GO-ATeam2* knock-in mice. After piercing the fibroblast membrane, we applied different concentrations of ATP, monitored the FRET ratio, and determined coefficients based on the function for fitting ATP concentration to the FRET ratio. Second, we performed a luciferase assay of ATP concentration (Tissue ATP assay kit; TOYO B-NET) in fertilized eggs from *GO-ATeam2* knock-in mice. Mice were injected with ATP synthetase inhibitors (2DG plus antimycin A), and the time course of the FRET ratio was monitored. Coefficients obtained by the two methods were substantially identical, indicating that they were appropriate for use in the present study. *In vivo* ATP imaging was performed using fluorescence microscopy and two-photon microscopy, as previously reported (Yamamoto et al., 2019; Ohnishi et al., 2021). Briefly, *GO-ATeam2* knock-in rats or mice were anesthetized with 2% isoflurane, and sciatic nerves were exposed and photographed under general anesthesia. A blackout curtain was placed around the nerve during photography to prevent the epineurium and fibrofatty tissue from interfering with ATP levels. Photographs were taken at designated times for each experiment. We used both *GO-ATeam2* knock-in rats and mice for fluorescence microscopy (M165 FC; Leica Microsystems). An exciting light (470/40 nm, 2.5 W under objective lens) was applied, and a

dichroic mirror 540 DCLP of 515/30 and 575/40 was used for GFP and OFP emission (DualView2 filter sets, INDEC Biosystems). The exposure time was 1000 ms. Fluorescence emission in the *GO-ATeam2* probe was captured using a CCD camera (ORCA-Flash 4.0, Hamamatsu Photonics KK Shizuoka), which could evaluate whole nerve ATP levels. We used only *GO-ATeam2* knock-in mice for two-photon microscopy (A1R MP+; Nikon) because the size of the mouse was suitable for imaging. Exciting light (920 nm, 20 W under objective lens) was applied, BP525/50 filters were used for emission, and DM560 and DM640 filters were used for excitation fluorescence separation. For the center of the longitudinal nerve cross-section of the sciatic nerve, fluorescence emission in the *GO-ATeam2* probe was captured. For fluorescence and two-photon microscopy, the imaging data were analyzed using MetaMorph software (Molecular Devices). For FRET signals at the chosen region of interest (ROI), OFP/GFP ratios were calculated with subtraction of the background signal to normalize the background condition. We set different ROI for each animal species or microscope. Six 1 × 1-mm square ROIs were chosen for fluorescence microscopy in rats, three proximal and three distal to the sectional end, with 500- $\mu$ m spacing for each ROI (Extended Data Fig. 1-1). For fluorescence microscopy in mice, 3 mm distal from the sectional end, with a 500 × 500- $\mu$ m square ROI, was chosen (Extended Data Fig. 7-2). For two-photon microscope experiments in mice, to avoid the interference of the epineurium or fibrofatty tissue unrelated to internal nerves, 3 mm distal from the sectional end, the center of the longitudinal nerve cross-section, with a 300 × 300- $\mu$ m square ROI was chosen (Extended Data Fig. 3-1). Fluorescence microscopy imaging reflects whole nerve ATP levels, and two-photon microscopy imaging reflects the longitudinal nerve cross-section ATP levels. The same individuals were used for fluorescence microscopy until 120 min (Extended Data Fig. 7-1) or 360 min (Fig. 1a,b) after axotomy, and the separate individuals were used for the other experiments including fluorescence and two-photon microscopy. This was because of the restrictions on the length of time of guidelines of our institute that animals were allowed to be kept outside of the animal laboratory.

### Myelinated axon measurement

Tissue preparation was performed 3 mm distal to the sectional end for the injured nerves and contralateral uninjured nerves. Samples were fixed in 2.5% glutaraldehyde in 0.1 M cacodylate buffer (pH 7.4) overnight at 4°C, post-fixed with 1% OsO<sub>4</sub> and embedded in epoxy resin. Semithin cross-sections (1  $\mu$ m) were stained with an aqueous solution containing 0.5% toluidine blue and scanned using an epifluorescent microscope (BZ-X700, Keyence). Ultrathin sections (90 nm) were scanned using a transmission electron microscope (H-7500; Hitachi). Histologic quantification was conducted using epifluorescent microscopy by a blinded investigator using established non-biased counting methods (Beirowski et al., 2005; Babetto

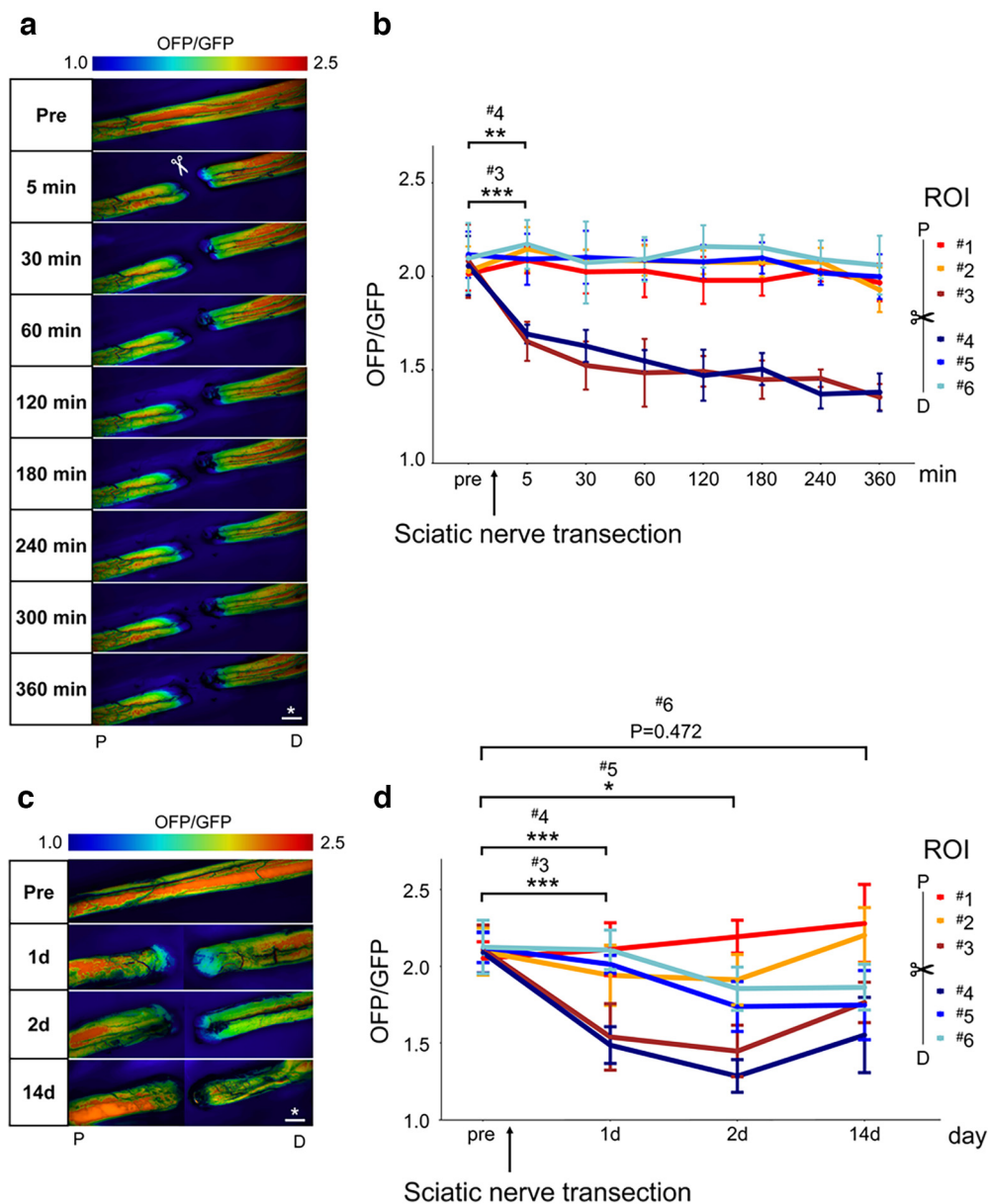


**Figure 1.** Spatiotemporal change for rat sciatic nerve whole ATP levels with fluorescence microscope after axotomy. **a**, Representative whole nerve intracellular ATP images before (pre) and 5, 30, 60, 120, 180, 240, 300, and 360 min after axotomy in the same individuals. Scale bar, \* 1 mm. P, proximal. D, distal. **b**, The change of ATP levels with six ROIs (from ROI #1 to #6;  $n=4$  rat per group). Distal nerve stump ATP levels (ROI #5 and #6) were maintained over 360 min. **c**, Representative whole nerve intracellular ATP images before (pre), and 1 d (24 h), 2 d (48 h), and 14 d after axotomy in the separate individuals. Scale bar, \* 1 mm. P, proximal. D, distal. **d**, The change of ATP levels with six ROIs (from ROI #1 to #6;  $n=6$  rat per group). Distal nerve stump ATP levels (ROI #5 and #6) were significantly decreased from 2 d after axotomy. The ROI for measuring ATP levels was set on six regions: three proximal (from ROI #1 to #3) and three distal (from ROI #4 to #6) sites for axotomy, and a 1-mm square with 500- $\mu$ m spacing (Extended Data Fig. 1-1). The OFP/GFP ratios ranged from 1.0 to 2.5. Error bars indicate SD; \* $p < 0.05$ , \*\* $p < 0.01$ , \*\*\* $p < 0.001$ , two-way ANOVA followed by the Tukey's *post hoc* test. ROI, region of interest.

et al., 2013; Viader et al., 2013; Sasaki et al., 2018). Briefly, whole sciatic nerve semi-thin section was imaged at 100 $\times$  magnification with tile scanning, and the total area of the nerve was measured (BZ-X700 Analyzer, Keyence). Then, four randomly selected images were imaged (108  $\times$  144  $\mu$ m) at 1000 $\times$  magnification with using oil-immersion lens, and intact myelinated axons were

counted (ImageJ; v1.52p, and Cell Counter Plugin) in each image. Finally, based on the total area and the number of intact myelinated axons measured in each image, the number of axons in the entire nerve was estimated. The survival criteria for intact axons were normal myelin sheaths, uniform axoplasm, and intact mitochondria, as per the electron microscope findings described below.

### G-ratio calculation, mitochondrial diameter, and atypicality

Ultrathin sciatic nerve cross-sections (90 nm) were analyzed for mitochondrial diameter or atypicality, axon diameter, and G-ratio (the ratio between the inner axon and outer myelin perimeter) by electron microscopy. For myelinated axons, the inner and outer diameters of the myelin sheath were measured from 100 fibers randomly selected from four individuals per group using the GRatio software plug-in, available online (<http://gratio.efil.de>), implemented in ImageJ (<https://imagej.nih.gov/ij/>), which allowed semi-automatic G-ratio calculation (Beirowski et al., 2017; Roberts et al., 2017; Alvarez-Prats et al., 2018). The mean G-ratio was calculated for each individual. Fifty mitochondria from each of the four individuals were measured in cross-sections, and the mean mitochondrial diameter was calculated for each individual (Barrientos et al., 2011). We defined atypical mitochondria as having a swollen shape, vacuolization or cavitation of the matrix, and lack of continuity in the outer and inner membranes (Lenzi et al., 2012; Natale et al., 2015; Chen et al., 2017).

### Immunohistochemistry

The frozen section procedure was performed 3 mm distal to the injured nerves' sectional end and the contralateral uninjured nerves. Sciatic nerves from mice or rats were fixed in 4% paraformaldehyde/0.1 M PBS overnight, sucrose gradient (10%, 20%, 30% in 1× PBS), embedded in Tissue-Tek O.C.T. compound (Tissue Tek, Sakura Finetek Japan Co, Ltd.), and sectioned at 10 μm on a cryostat (CM3050 S, Leica Microsystems). Samples were washed in 1× PBS for 20 min and then blocked with 1% ECL Prime Blocking Reagent in 0.1% Triton X-100 1× PBS for 1 h at room temperature. Sections were incubated in primary antibodies in blocking/permeabilized solution overnight at 4°C, washed in 1× PBS for 10 min, and incubated with secondary antibodies for 1 h at room temperature. Samples were washed twice in 1× PBS for 15 min and mounted in VECTASHIELD Antifade Mounting Medium containing DAPI (H-1200, Vector Laboratories). The following primary and secondary antibodies and these concentrations were used as follows: Mouse-Monoclonal Anti-NF-H, 1:1000, NBP1-05210, Novus Biologicals; Rabbit polyclonal antibody Anti-S-100B, 1:500, GTX129573, Genetex; Rat-Monoclonal Anti-CD-68, 1:100, 14-0681-82, Invitrogen; Mouse-Monoclonal Anti-HK1, 1:100, sc-46695, Santa Cruz Biotechnology Inc; Mouse-Monoclonal Anti-PFK1, 1:100, sc-377346, Santa Cruz Biotechnology Inc; Mouse-Monoclonal Anti-LDHA, 1:100, sc-137243, Santa Cruz Biotechnology Inc; Mouse-Monoclonal Anti-LDHB, 1:100, sc-100775, Santa Cruz Biotechnology Inc; Mouse-Monoclonal Anti-MCT-1, 1:500, GT14612, Genetex; Mouse-Monoclonal Anti-MCT-4, 1:100, sc-376140, Santa Cruz Biotechnology Inc; Mouse-Monoclonal Anti-PDH-E1 $\alpha$ , 1:100, sc-377092, Santa Cruz Biotechnology Inc; Mouse-Monoclonal Anti-citrate synthase, 1:100, sc-390693, Santa Cruz Biotechnology Inc; Mouse-Monoclonal Anti-IDH3A, 1:100, sc-398021, Santa Cruz Biotechnology Inc; DyLight 488 Goat anti-mouse IgG H&L, 1:1000, DI-1488, Vector Laboratories; DyLight 549 Goat anti-rabbit IgG H&L, 1:1000,

DI-1549, Vector Laboratories; Alexa Fluor 488 Goat anti-rat IgG H&L, 1:1000, ab150157, Abcam. A laser scanning confocal microscope system (Zeiss LSM710; Carl Zeiss) was used to acquire images. The cross-section images of 63× magnification (135 × 135 μm) were used to measure quantitative Schwann cell counts and axonal fluorescence intensity. HK1, PFK1, MCT1, and MCT4/S-100B/DAPI co-positive cells were measured under four fields as HK-1/PFK-1/LDHA/LDHB/MCT-1/MCT-4 positive Schwann cells, and the total number of cells was counted. The axonal fluorescence intensity of HK-1, PFK-1, LDHA, LDHB, PDH-E1 $\alpha$ , CS, and IDH3A were measured by using ImageJ, as previously described (Jia et al., 2021). Briefly, the average intensity within 100 axons surrounded by Schwann cells (S-100B) per mouse was measured with subtraction of the background intensity. Imaging analyses were performed in a blinded manner regarding the treatment status of the nerve. All others were observed in each of the three sections of at least three individuals.

### Mass spectrometry

Transection was performed on the right side, whereas the uninjured contralateral left side was used as a control. The entire distal sciatic nerve stump was analyzed at a continuous distance of 7 mm from the sectional end. The tissue samples were dissolved in ice-cold 80% methanol at a concentration of 100 mg/ml, sonicated five times (30 s of sonication and 30 s of cooling) using a BIORUPTOR (Cosmo Bio Co, Ltd), and centrifuged at 21,500 × *g* for 5 min at 4°C. The supernatant fluids were evaporated to dryness. After dissolving in 50 μl of 0.1% formic acid, the samples were subjected to liquid chromatography mass spectrometry analysis. Metabolites in the glycolytic system, TCA cycle, ATP, and NAD<sup>+</sup> were analyzed employing liquid chromatography-mass spectrometry using LCMS-8040 instruments (Shimadzu). The sample was separated by reverse phase ion-pair chromatography using an ACQUITY UPLC BEH C18 column (100 × 2.1 mm, 1.7-μm particle size, Waters). The mobile phase consisted of solvent A (15 mM acetic acid and 10 mM tributylamine in 3% methanol) and solvent B (methanol), and the column oven temperature was 40°C. The gradient elution program was as follows: a flow rate of 0.3 ml/min: 0–3 min, 0% B; 3–5 min, 0–40% B; 5–7 min, 40–100% B; 7–10 min, 100% B; 10.1–14 min, 0% B. Parameters for the negative electrospray ionization source (ESI) mode under multiple reaction monitoring (MRM) were as follows; drying gas flow rate, 15 l/min; nebulizer gas flow rate, 3 l/min; DL temperature, 250°C; and heat block temperature, 400°C; collision energy (CE), 230 kPa. Data processing was conducted using the LabSolutions LC-MS software (Shimadzu).

### Local administration of inhibitor

Several inhibitors were locally administered to the sciatic nerve, as described in a previous report (Chung et al., 2019). A schematic illustration of the experimental design is shown in Extended Data Figure 7-1a. Briefly, under

general anesthesia, the bilateral sciatic nerves of *GO-ATeam2* mice were exposed and only the right sciatic nerve was cut (transection side). Immediately after axotomy, the distal nerve stump was covered with a gelatin sponge (873322, LTL Pharma) soaked with inhibitors and a 3-mm PVC tube to prevent leakage of the solution, whereas the left intact sciatic nerve was only covered with a gelatin sponge soaked with inhibitors (sham side). The fascia and skin were then sutured tightly. One day (24 h) after the surgical procedure, ATP imaging with two-photon microscopy or harvesting of sciatic nerve lesions was performed. All procedures were performed under a stereomicroscope (L-0950D; Inami Corporation). We used 2-Deoxy-D-glucose (2-DG) as the indirect hexokinase (HK) inhibitor, MSDC-0160 as the mitochondrial pyruvate carrier (MPC) inhibitor, and *α*-cyano-4-hydroxycinnamic acid (4-CIN) as a comprehensive inhibitor of MCTs (Extended Data Fig. 7-1*b*). Before proceeding to the main experiment, we preliminarily measured the change of ATP levels in the distal nerve stump for 120 min intermittently, by using two concentrations of all inhibitors (Extended Data Fig. 7-1*c,d*). The concentrations of inhibitors were determined from previous studies (Press and Milbrandt, 2008; Miranda-Goncalves et al., 2013; Tsuyama et al., 2013; Patterson et al., 2014; Anamitra Ghosh, 2016; Ichihara et al., 2017; Babetto et al., 2020). Then, we used higher concentrations for all inhibitors in the main experiments. The concentrations of the inhibitors were 150 mM 2DG (D8375, Sigma-Aldrich), 100  $\mu$ M MSDC-0160 (HY-100550, Med Chem Express), and 10 mM 4-CIN (70990, Sigma-Aldrich). For all inhibitors, the solvent was dimethyl sulfoxide (DMSO) diluted to a 0.1% concentration with saline, and only the DMSO group was used as the solvent.

### Local administration of EP

Ethyl pyruvate (EP; 051-05292, Wako) was used because of the poor stability of pyruvate, and the concentrations were applied at 3, 10, 30, and 100 mM based on previous reports (Park et al., 2015; Chung et al., 2019). The method of topical administration was the same as that of the inhibitor. Briefly, under general anesthesia, the right sciatic nerve was exposed and performed axotomy. Immediately after the axotomy, the distal nerve stump was covered with a gelatin sponge soaked with EP, diluted with saline as the solvent. Only saline was defined as the saline group. Two days (48 h) after the surgical procedure, ATP imaging with two-photon microscopy or harvesting of sciatic nerve lesions was performed.

### Statistical analysis

Statistical analysis was performed using EZR (version 1.40, Saitama Medical Center, Jichi Medical University, Saitama, Japan), a graphical user interface for R (version 4.0.4, The R Foundation for Statistical Computing). Sample sizes were selected based on those generally used in this research field. Data sets with a normal distribution and equal variances are presented as mean  $\pm$  SD, whereas the others are represented as mean and interquartile ranges. A

two-tailed *t* test, Spearman's  $\rho$  correlation coefficient and spearman test, or Mann-Whitney *U* test was used to compare two groups according to the distribution and variance of the data. One-way ANOVA followed by Tukey's *post hoc* test was used to compare more than two groups. Two-way ANOVA followed by Tukey's *post hoc* test was used to compare the data, which were affected from two different factors. In all statistical analyses, *p* values <0.05 were considered significant.

### Data accessibility statement

The data that support the findings of this study are available from the corresponding author on reasonable request.

## Results

### Spatiotemporal decrease of ATP levels in the distal nerve stump and mitochondrial degeneration in axon

To clarify the changes in intracellular ATP in WD, we first examined ATP levels in the *GO-ATeam2* knock-in rat sciatic nerve transection model. In the six ROIs, we measured whole-nerve ATP levels intermittently until 360 min after axotomy in the same individuals (Fig. 1*a,b*). Distal nerve stump ATP levels (ROI #5 and #6) did not decrease for 360 min (Fig. 1*a,b*). Only the sectional end (ROIs #3 and #4) revealed a significant decrease in ATP levels 5 min after axotomy (Fig. 1*a,b*).

Next, we measured ATP levels before (pre), 1 d (24 h), 2 d (48 h), and 14 d after axotomy in separate individuals (Fig. 1*c,d*). Two days after axotomy, distal nerve stump ATP levels (ROI #5) showed a significant decrease (Fig. 1*c,d*). The most distal (ROI #6) ATP levels showed a decreasing tendency, but not significant (Fig. 1*c,d*). We also evaluated the histology 3 mm distal from the sectional end (Extended Data Fig. 1-1, corresponding to ROI #6). Two days after axotomy, the number of myelinated axons significantly decreased (Fig. 2*a,b*), and the G-ratio significantly increased (Fig. 2*a,c,d*), indicating WD progression. These findings suggest that the decrease in ATP levels is associated with histologic progression of WD in the distal nerve stump.

To examine the primary ATP source in the distal nerve stump, we evaluated mitochondrial diameter and atypicality. The main component units of the sciatic nerve were evaluated separately in the axons and Schwann cells. In axons, mitochondria showed enlarged diameters and progressed atypicality from 1 d after axotomy, whereas in Schwann cells, they showed critical and significant change between 2 and 14 d (Fig. 2*e-g*). These findings indicated that the distal nerve stump caused the mitochondrial degeneration in axons.

### Gradual decrease of ATP levels in the distal nerve stump and axonal degeneration

Next, to assess ATP levels of the sciatic nerve components in the distal nerve stump, we performed the two-photon microscopic analysis in the center of the longitudinal section before (pre), 1 d (24 h), 2 d (48 h), and 7 d after axotomy of *GO-ATeam2* knock-in mice. Two-photon microscopy

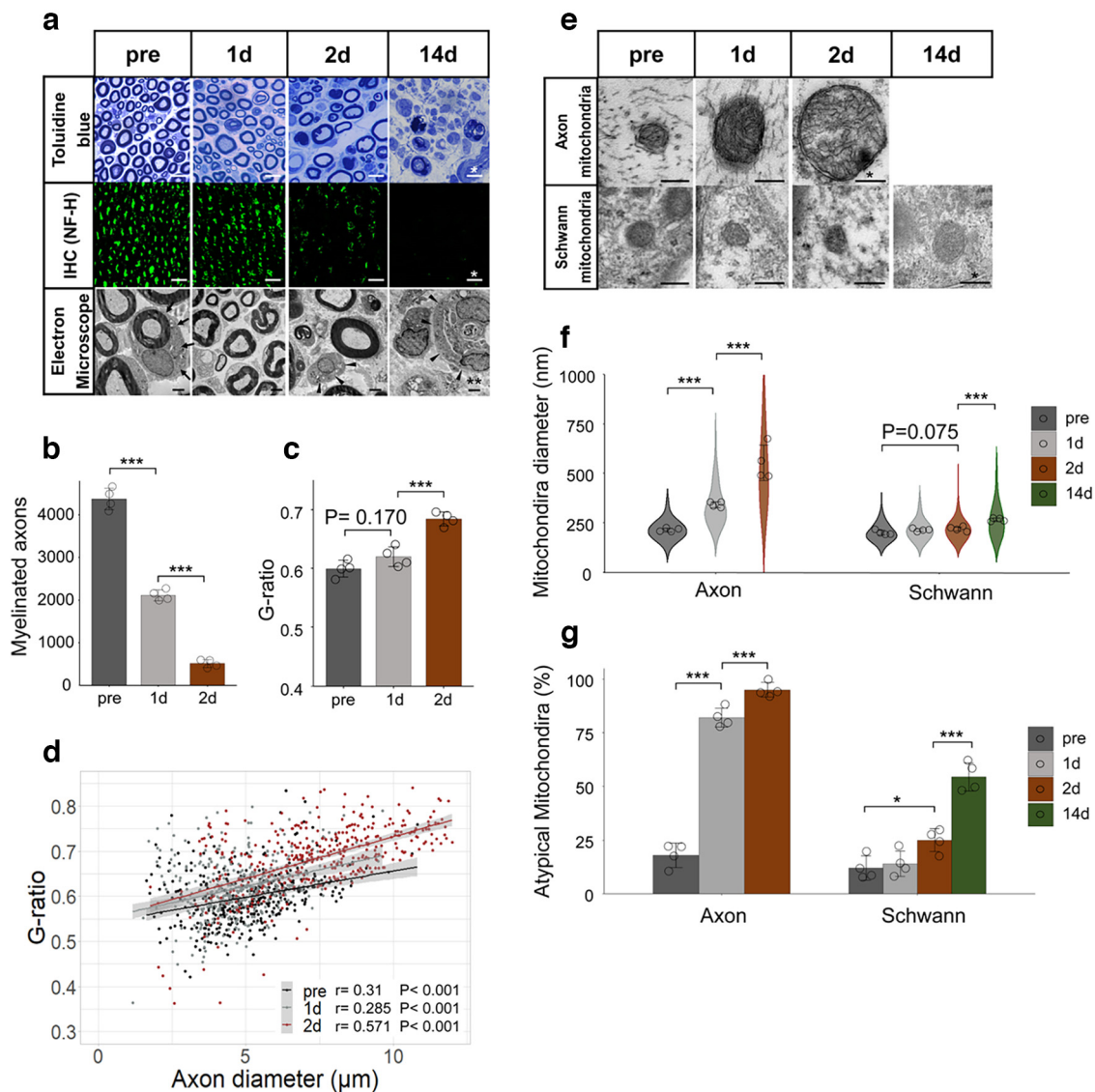


**Figure 2.** Wallerian degeneration and mitochondrial degeneration in axon for rat's distal nerve stump. **a**, Representative images of toluidine blue staining, immunohistochemistry (NF-H), electron microscopy, before (pre) and 1, 2, and 14d after axotomy. Immunohistochemistry was obtained the same results for three individuals. Scale bar, \* 10  $\mu$ m, \*\* 2  $\mu$ m. Arrows, myelinated axon; arrowheads, demyelinated Schwann cell. **b**, Quantification of the myelinated axon. **c**, **d**, Quantification of the G-ratio [**c**: cumulative G-ratio per individual, **d**: scatter plot, Spearman's rank correlation coefficient and *p* values showing G-ratio of individual myelinated axons against axon diameter (*n* = 400)]. The histologic WD was observed significantly from 2 d after axotomy. In axons, before (pre) and 1 and 2 d after axotomy were evaluated, except for after 14 d with completely collapsed axon morphology (*n* = 4 rat per group). **e**, Representative images of mitochondrial findings, before (pre) and 1, 2, and 14 d after axotomy. Evaluation was performed in axons and Schwann cells separately. Scale bar, \* 200 nm. **f**, Violin plot of mitochondrial diameter (nm; *n* = 200). Cumulative mitochondria diameter per individual are also shown (*n* = 4 rat per group). **g**, Quantitative analysis of atypical mitochondria (%; *n* = 4 rat per group). In axons, mitochondria were significantly degenerated from 1 d after axotomy, whereas in Schwann cells, mitochondria were not significantly degenerated until 14 d after axotomy. All histologic evaluations were performed 3 mm distal to the sectional end and corresponding uninjured nerve. Error bars indicate SD; \**p* < 0.05, \*\*\**p* < 0.001, one-way ANOVA followed by the Tukey's *post hoc* test (for comparison of axons and Schwann cells, respectively).

allow us to remove interference with ATP levels by epineurium tissue. We measured intracellular ATP levels 3 mm distal from the sectional end with a 300  $\times$  300- $\mu$ m square ROI. The distal nerve stump ATP levels showed a gradual and significant decrease (Fig. 3a,b). The immunohistochemistry for neurofilament and toluidine blue staining presented the low detection and fragmentation, indicating

the axonal degeneration over time 2 d after axotomy (Fig. 3c, double arrows). However, S-100B-positive Schwann cell bodies were detected up to 7 d after axotomy (Fig. 3c, arrowhead). We also detected infiltrated CD68 macrophages 2 d after axotomy (Fig. 3c, arrow). Although the sciatic nerve components included in axons, Schwann cells, and macrophages 2 d after axotomy, we could not

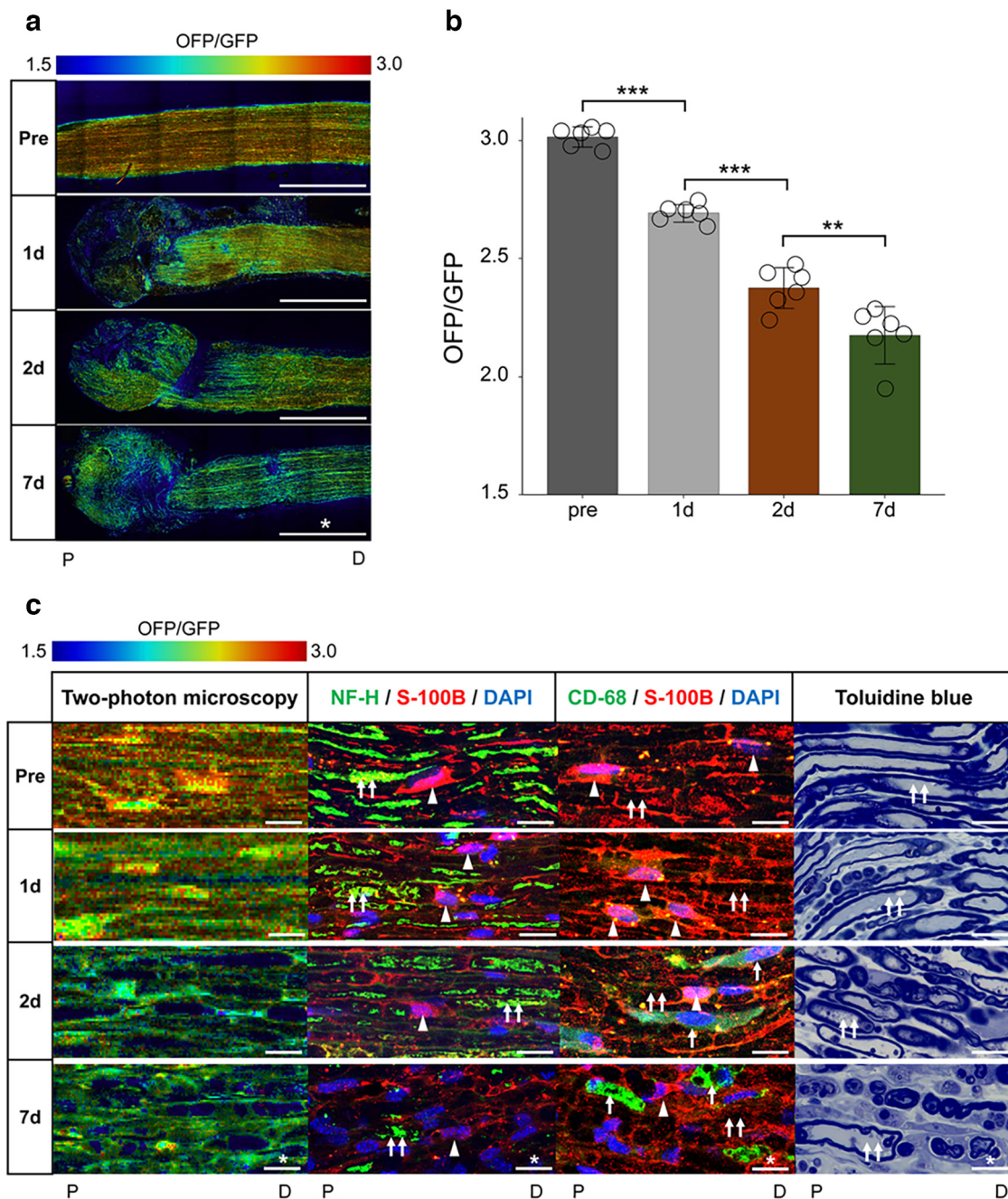


**Figure 3.** The gradual decrease of mice longitudinal nerve cross section ATP levels in the distal nerve stump, corresponds to histology. **a**, Representative ATP images in the longitudinal section before (pre) and 1, 2, and 7 d after axotomy. Scale bar, \* 1 mm. P, proximal. D, distal. **b**, The change of ATP levels with measured ROIs ( $n=6$  mice per group). Distal nerve stump ATP levels were significantly decreased from 1 d after axotomy. Error bars indicate SD; \*\* $p < 0.01$ , \*\*\* $p < 0.001$ , one-way ANOVA followed by the Tukey's *post hoc* test. **c**, Representative enlarged images of two-photon microscopy, immunohistochemistry (left, NF-H/S-100B/DAPI; right, CD68/S-100B/DAPI), and toluidine blue staining, before (pre) and 1, 2, and 7 d after axotomy. Scale bar, \*  $10 \mu\text{m}$ . Arrows, macrophage; arrowheads, Schwann cell; double arrows, axonal soma. The ROI for measuring ATP levels was set at 3 mm distal from the sectional end, the center of the longitudinal cross-section, with a  $300 \times 300\text{-}\mu\text{m}$  square (Extended Data Fig. 3-1). The OFP/GFP ratios ranged from 1.5 to 3.0. All histologic evaluations were performed with the same results for three individuals, 3 mm distal from the sectional end, and the corresponding uninjured nerve. ROI, region of interest.

detect the specific components with ATP levels same as preaxotomy (Fig. 3c). These findings suggested that a gradual decrease in ATP levels in the distal nerve stump was preceded by WD.

#### Activation of the glycolytic system after axotomy

The main metabolic pathways of ATP production include the glycolytic system in the cytoplasm and the TCA cycle in the mitochondria. To clarify the ATP production



pathway in the distal nerve stump, we performed mass spectrometry for energy metabolites before (pre) and 2 d (48 h) after axotomy. The metabolites of the glycolytic system, glucose, glucose-6-phosphate (G6P), fructose 6-phosphate (F6P), glyceraldehyde-3-phosphate (GA3P), and pyruvate, showed a significant decrease after axotomy (Fig. 4, upper square). However, lactate, which is reversible metabolite from pyruvate, showed a nonsignificant decrease. These results suggested that the distal stump activated the glycolytic pathway.

Under aerobic conditions, the MPC transports pyruvate from the cytoplasm to the mitochondria for metabolism in the TCA cycle (Bricker et al., 2012; Halestrap, 2012). Metabolites of the first part of the TCA cycle in the mitochondria, citrate and isocitrate showed nonsignificant decrease while  $\alpha$ -ketoglutaric acid showed significant decrease after axotomy (Fig. 4, lower square). ATP and  $\text{NAD}^+$  levels showed a significant decrease after axotomy (Fig. 4). Mass spectrometry also showed a decrease in ATP levels in the distal nerve stump, consistent with the results of our *in vivo* imaging.

### Schwann cells activate the glycolytic system and monocarboxylate transport after axotomy

The mass spectrometry could not evaluate the respective metabolic changes of Schwann cells and axons as it reflected the whole intracellular changes of the distal nerve stump. Therefore, we next performed immunohistochemical evaluation with cell type-specific antibodies and metabolic enzymes.

In Schwann cells, we evaluated the activity of glycolytic system and MCTs after axotomy. We performed immunohistochemical analysis for glycolytic enzymes (HK-1, hexokinase 1; PFK-1, phosphofructokinase 1; LDHA, lactate dehydrogenase A subunit; LDHB, lactate dehydrogenase B subunit) and MCTs (1/4) before (pre) and 2 d (48 h) after axotomy, and measured the number of glycolytic enzymes and MCT-positive Schwann cells. HK-1, PFK1, and LDHA positive Schwann cells showed a significant increase after axotomy (Fig. 5a–f). MCT-1 and MCT-4 positive Schwann cell numbers also showed a significant increase (Fig. 5i–l). However, LDHB positive Schwann cells showed a significant decrease after axotomy (Fig. 5g,h). LDHA is the enzyme that converts pyruvate to lactate and  $\text{NAD}^+$ , whereas LDHB is the enzyme that reacts in the opposite direction (Doherty and Cleveland, 2013), and  $\text{NAD}^+$  is used for working glycolysis (Fantin et al., 2006; Diaz-Garcia et al., 2017; Urbanska and Orzechowski, 2019; Osis et al., 2021). These results suggest that the glycolytic system in Schwann cells and MCT-induced monocarboxylate transport to axons were activated in the distal nerve stump.

### Axons activate the glycolytic system and inactivate the TCA cycle after axotomy

In axons, we evaluated the activity of glycolytic system and TCA cycle after axotomy. We performed immunohistochemical analysis for glycolytic enzymes (HK-1, PFK-1, LDHA, LDHB), and TCA cycle enzymes (PDH, pyruvate dehydrogenase; CS, citrate synthase; IDH, isocitrate dehydrogenase)

before (pre) and 2 d (48 h) after axotomy, and measured the fluorescence intensity within axons surrounding Schwann cell-specific staining (S-100B). Interestingly, the relative intensity of HK-1, PFK1, and LDHA showed a significant increase after axotomy (Fig. 6a–f). Conversely, the relative intensity of LDHB, PDH-E1 $\alpha$ , CS, and IDH3A showed a significant decrease after axotomy (Fig. 6g–n). In the distal nerve stump, we showed that the glycolytic system was activated not only in Schwann cells but also in axons. Furthermore, TCA cycle was inactivated in axons. These results suggest that even in axons, the metabolic source of ATP is mainly on glycolytic system in the distal nerve stump. This theory is also supported from mitochondrial degeneration in axons (Fig. 2e–g).

### Inhibition of the glycolytic system and MCT-induced monocarboxylate transport decrease ATP levels and progress WD after axotomy, whereas TCA cycle does not

In the distal nerve stump, we showed that Schwann cells activate the glycolytic system and MCT-induced monocarboxylate transport, axons inactivate TCA cycle while activating the glycolytic system, resulting a gradual decrease in ATP levels. Then, we hypothesized that the inhibition of the glycolytic system and MCT-induced monocarboxylate transport progress WD, whereas the inhibition of the TCA cycle did not. To prove this hypothesis, we performed *in vivo* inhibitor experiments. We tried several energy metabolic inhibitors to axotomized right sciatic nerve (transection side) and served left (sham side), and evaluated progressive WD after 1 d (24 h).

First, we performed a 2-DG treatment to inhibit the glycolytic system. The 2-DG group showed a further decrease in ATP levels on both the sham and transection sides compared with the DMSO group (Fig. 7a,b). The 2-DG group also showed a decrease in the number of myelinated axons and an increase in the G-ratio on both sides (Fig. 7c–g). On both sides, the 2-DG group also showed an increase in MCT1-positive Schwann cells (Fig. 7h,i). In addition, only on the sham side of the 2-DG group show a progression of mitochondrial atypicality (Fig. 7j,k). Interestingly, the transection side of the 2-DG group did not show further progression of mitochondrial atypicality in Schwann cells and axons (Fig. 7j,k). In the distal nerve stump, inhibition of the glycolytic system decreased ATP levels and progressed WD but had nominal effect on mitochondrial degeneration in axons.

Next, we performed MSDC-0160 treatment to inhibit MPC. On the sham side, the MSDC-0160 group showed a decrease in ATP levels (Fig. 7a,b) and a decrease in the number of myelinated axons, compared with the DMSO group (Fig. 7c–g). However, on the transection side, MSDC-0160 showed neither decrease in ATP levels (Fig. 7a,b) nor decrease number of myelinated axons and increase in G-ratio (Fig. 7c–g). On both sides, the MSDC-0160 group also showed an increase in MCT1-positive Schwann cells (Fig. 7h,i). On the sham side, the MSDC-0160 group showed progression of mitochondrial atypicality in Schwann cells, and axons (Fig. 7i,j). On the transection side, the MSDC-0160 group showed a further progression of mitochondrial

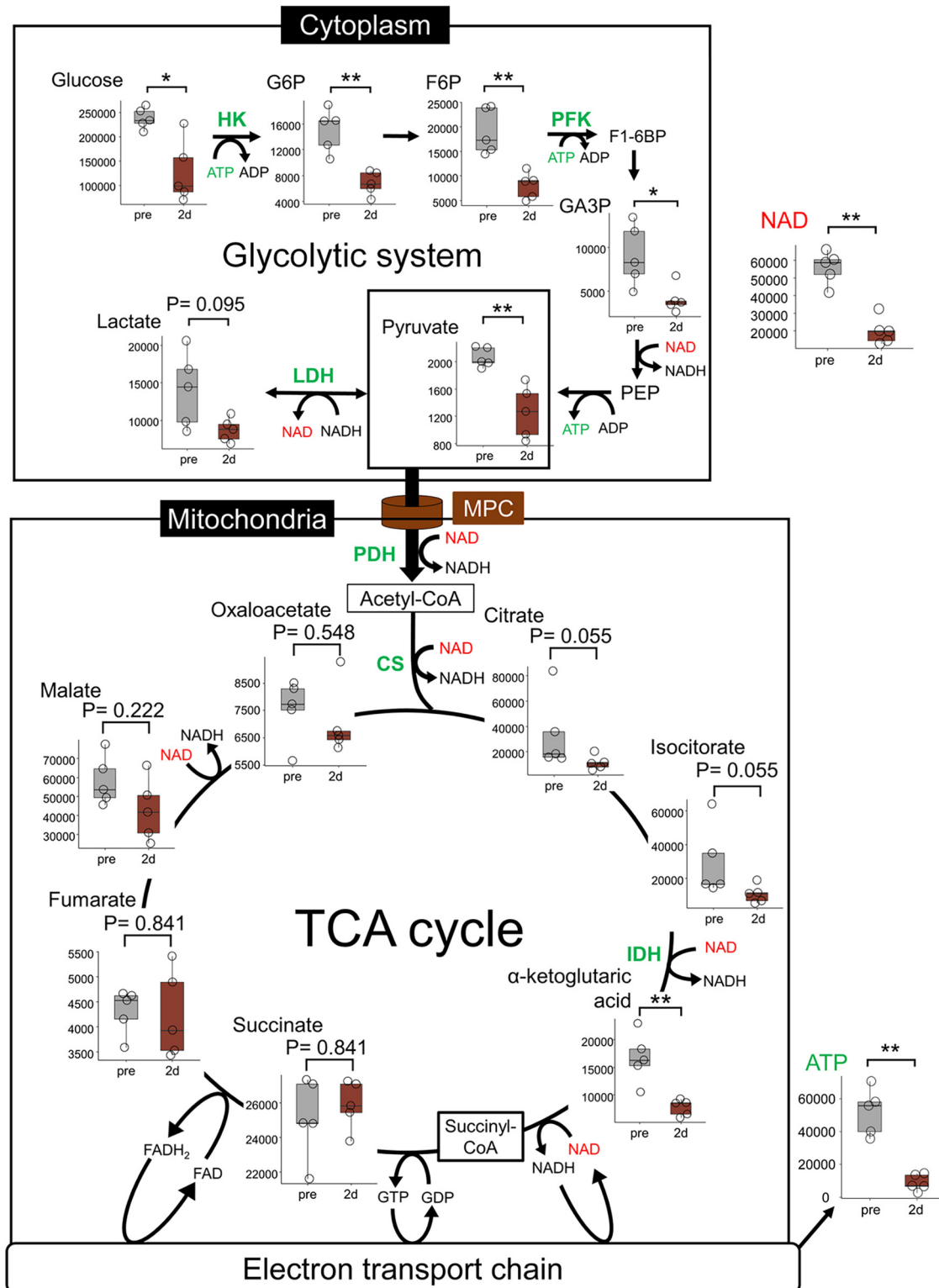


**Figure 4.** Activation of the glycolytic system. Diagram of energy metabolism pathways and mass spectrometry before and 2 d (48 h) after axotomy. MPC transports pyruvate, the end-product of the glycolytic system, for metabolism in the TCA cycle. Mass spectrometry was performed for the metabolites of glycolysis and the TCA cycle, the end-product ATP, and the coenzyme NAD<sup>+</sup>. Glycolytic intermediates, NAD<sup>+</sup> and ATP were significantly decreased after axotomy. These results are shown in a boxplot containing the interquartile range and centered bars as the median ( $n = 5$  mice per group). All examinations were performed continuously 7 mm from the sectional end of the right sciatic nerve with transection and the corresponding lesion on the left side. \* $p < 0.05$ , \*\* $p < 0.01$ , Mann-Whitney  $U$  test. CS, citrate synthase; F6P, fructose 6-phosphate; G6P, glucose-6-phosphate; GA3P, glyceraldehyde-3-phosphate; HK, hexokinase; IDH, isocitrate dehydrogenase.

continued

isocitrate dehydrogenase; LDH, lactate dehydrogenase; NAD<sup>+</sup>, nicotinamide adenine dinucleotide; PFK, phosphofructokinase; PDH, pyruvate dehydrogenase; TCA cycle, tricarboxylic acid cycle.

atypicality in Schwann cells (Fig. 7i,j). These results revealed that the MPC inhibitor causes ATP depletion and WD progression only in uninjured nerves, but not in the distal nerve stump.

Finally, we performed 4-CIN treatment to inhibit MCT. On the transection side, the 4-CIN group showed a further decrease in ATP levels (Fig. 7a,b), a decrease in the number of myelinated axons, and an increase in the G-ratio compared with the DMSO or MSDC-0160 group (Fig. 7c-g). In particular, myelinated axons and the G-ratio showed the drastic progression of WD among all inhibitors (Fig. 7c-g). On both sides, the 4-CIN group also showed an increase in MCT1-positive Schwann cells (Fig. 7h,i), progression of mitochondrial atypicality in Schwann cells (Fig. 7i,j). The 4-CIN group showed further progression of mitochondrial atypicality in axons only on the transection side (Fig. 7i,j). These

results indicate that the MCT inhibitor most strongly progressed WD after axotomy and decreased ATP levels. However, the MCT inhibitor did not induce WD and decreased ATP levels before axotomy, suggesting that MCT-induced monocarboxylate transport is important after axotomy to supply energy metabolism.

In summary, on the transection side, inhibition of the glycolytic system and MCT progressed WD, whereas inhibition of MPC did not progress WD. On the sham side, inhibition of the glycolytic system and MPC progressed WD, whereas inhibition of MCT showed less WD progression. These findings supported that the metabolic source of ATP in the distal nerve stump was mainly depended on glycolytic system via MCT-induced monocarboxylate transport. A summary of the inhibition experiments is provided in Extended Data Table 7-1.

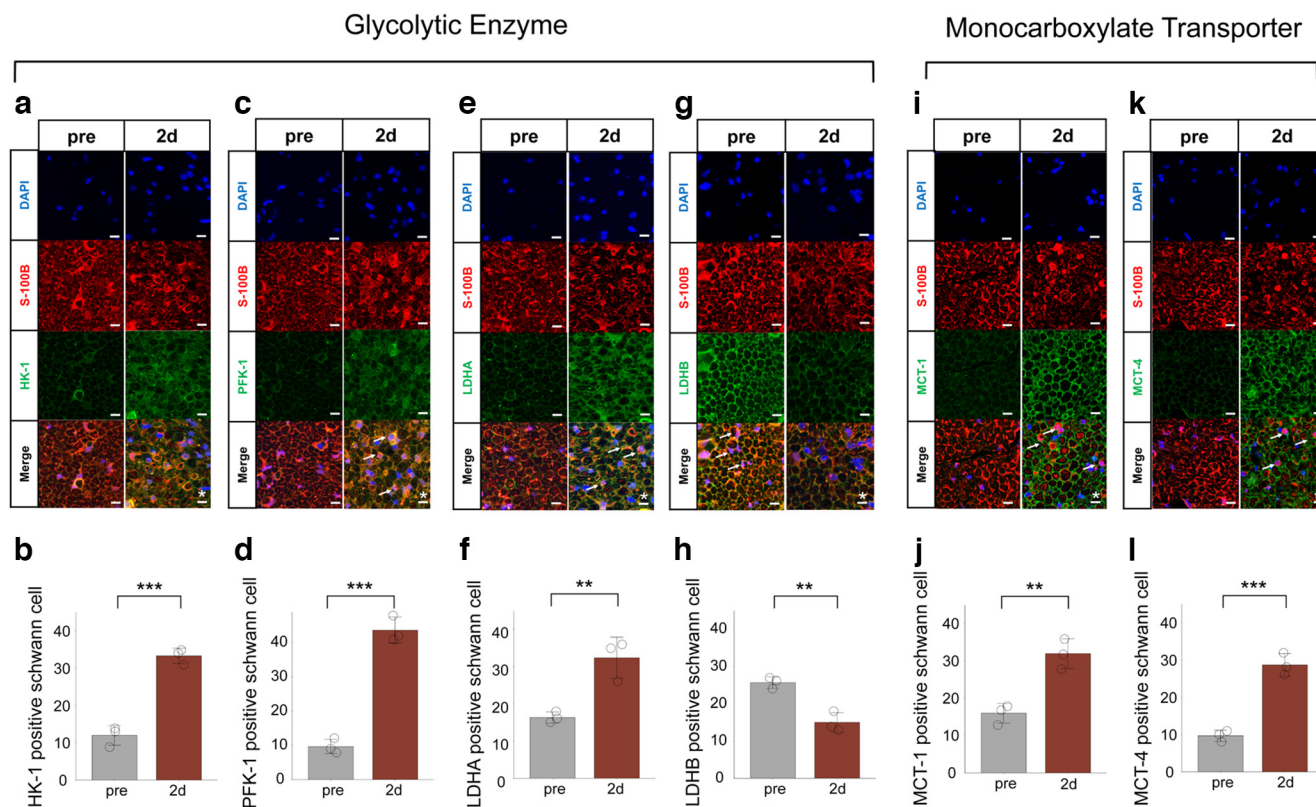


**Figure 5.** Activation of the glycolytic system and MCTs in Schwann cell after axotomy. **a, c, e, g**, Representative cross-section images of immunohistochemistry for glycolytic enzyme (**a**: HK-1, **c**: PFK-1, **e**: LDHA, **g**: LDHB) before and 2 d after axotomy. **b, d, f, h**, The number of HK-1 (**b**), PFK-1 (**d**), LDHA (**f**), and LDHB (**h**) positive Schwann cells ( $n=3$  mice per group). HK-1, PFK1, and LDHA positive Schwann cells were significantly increased after axotomy, whereas LDHB positive Schwann cells were significantly decreased. **i, k**, Representative images of immunohistochemistry for MCT (**e**: MCT-1, **g**: MCT-4) before and after axotomy. **j, l**, The number of MCT-1 (**j**) or MCT-4 (**l**) positive Schwann cells ( $n=3$  mice per group). MCT-1 and MCT-4 positive Schwann cells were significantly increased after axotomy. All histologic evaluations were performed 3 mm distal to the sectional end and corresponding uninjured nerve. Error bars indicate SD. Arrows, HK-1/PFK-1/LDHA/LDHB/MCT-1/MCT-4 positive Schwann cells; scale bar, 10  $\mu$ m. \* $p < 0.05$ , \*\* $p < 0.01$ , two-tailed  $t$  test. HK, hexokinase; LDHA, lactate dehydrogenase A subunit lactate; LDHB, lactate dehydrogenase B subunit lactate; dehydrogenase; MCT-1, monocarboxylate transporters 1; MCT-4, monocarboxylate transporters 4; PFK, phosphofructokinase.

## Glycolytic Enzyme

## TCA cycle Enzyme

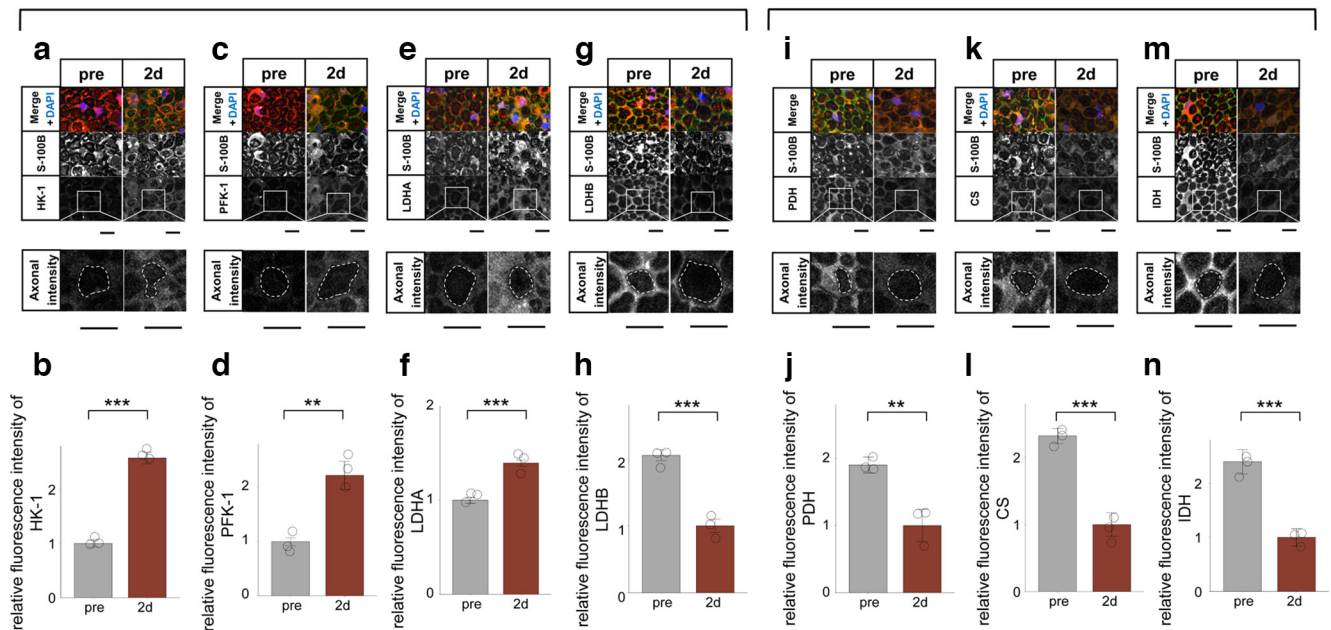


**Figure 6.** Activation of the glycolytic system and inactivation of the TCA cycle in axons after axotomy. **a, c, e, g**, Representative cross-section images of immunohistochemistry for glycolytic enzyme (**a**: HK-1, **c**: PFK-1, **e**: LDHA, **g**: LDHB) before and 2 d after axotomy. The axonal fluorescence intensity in the dashed line was measured. **b, d, f, h**, The axonal fluorescence intensity of HK-1 (**b**), PFK-1 (**d**), LDHA (**f**), and LDHB (**h**;  $n=3$  mice per group). HK-1, PFK1, and LDHA fluorescence intensity was significantly increased after axotomy, whereas LDHB was significantly decreased. **i, k, m**, Representative images of immunohistochemistry for TCA cycle enzyme (**i**: PDH-E1 $\alpha$ , **k**: CS, **m**: IDH3A) before and after axotomy. The axonal fluorescence intensity in the dashed line was measured. **j, l, n**, The axonal fluorescence intensity of PDH-E1 $\alpha$  (**j**), CS (**k**), and IDH3A (**n**;  $n=3$  mice per group). PDH-E1 $\alpha$ , CS, and IDH3A fluorescence intensity was significantly decreased after axotomy. All histologic evaluations were performed 3 mm distal to the sectional end and corresponding uninjured nerve. Error bars indicate SD scale bar, 10  $\mu\text{m}$ . \* $p < 0.05$ , \*\* $p < 0.01$ , \*\*\* $p < 0.001$ , two-tailed  $t$  test. CS, citrate synthase; IDH, isocitrate dehydrogenase; HK, hexokinase; LDHA, lactate dehydrogenase A subunit lactate; LDHB, lactate dehydrogenase B subunit lactate; dehydrogenase; PFK, phosphofructokinase; PDH, pyruvate dehydrogenase; TCA cycle, tricarboxylic acid cycle.

### EP supplementation activates MCT-induced transport resulting in delay WD

The results of inhibitor experiments also suggested that the glycolytic system is activated to sustain ATP levels in the distal nerve stump. We sought that supplementing pyruvate would contribute to delay WD through MCT-induced monocarboxylate transport and ATP production via the glycolytic pathway. Then, we tried EP supplementation immediately after axotomy and evaluated delayed WD after 2 d (48 h). Both the low (3 mM) and middle (10 mM) concentrations EP groups showed increased ATP levels compared with the saline group (Fig. 8a,b). The low (3 mM) concentrations EP group showed the most significant increase in ATP levels compared with the saline group. In contrast, the high (30 and 100 mM) concentrations EP group showed a decrease in ATP levels (data not shown). Both EP groups showed an increase in the number of myelinated axons, a decrease in the G-ratio (Fig. 8c–f), and an increase in MCT-1 positive Schwann cells (Fig. 8g,h). Finally, neither EP group showed improved mitochondrial atypicality in axons and Schwann cells (Fig. 8i–k). Together, these findings suggest that the pyruvate contribute to supplying ATP and delaying WD through glycolytic system.

### Discussion

Our study with spatiotemporal *in vivo* ATP imaging showed a gradually decreased levels of ATP in the distal nerve stump. In addition, we determined the metabolic source of ATP in degenerative axons with using mass spectrometry, histologic analysis, and pharmacological intervention. The glycolytic system both in Schwann cells and axons, and MCT-induced monocarboxylate transport were determined as the primary metabolic source of ATP following axotomy, which would delay WD. TCA cycle inactivation, in axons, gradually reduced ATP levels in the distal nerve stump, which indicates and is associated with WD progression.

In the PNS system, Schwann cells supply energy for the maintenance of axons (Beirowski et al., 2014; Nocera and Jacob, 2020; Stassart and Woodhoo, 2020). To evaluate precise ATP levels, ATP levels should be measured in axons and Schwann cells. Previous studies have used luciferase imaging, mass spectrometry, and magnetic resonance spectroscopy to measure intracellular ATP levels (Kennedy et al., 1999; Morikawa et al., 2012; Haris et al., 2014). However, these methods were unable to quantitatively measure ATP levels in real time or within different intracellular compartments. The ATP levels and

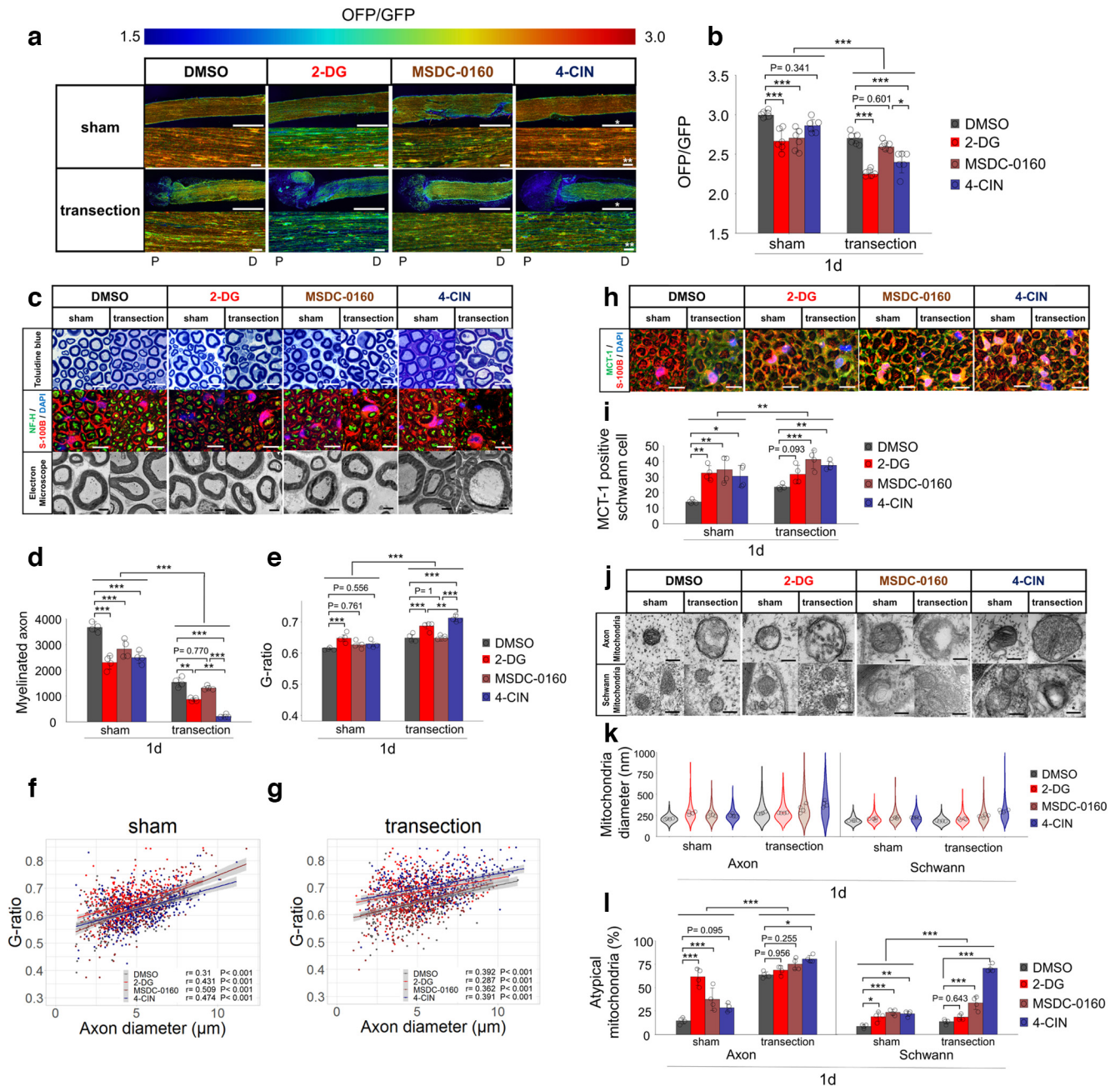


**Figure 7.** Inhibition of the glycolytic system or MCTs progress Wallerian degeneration with decreased ATP levels, but MPC does not. **a**, Representative ATP images for each inhibitor in both sham and transection side. For each experiment, lower figures are enlarged image with measured ROI. Upper figures present overall distal nerve stump ATP image, from the sectional end. Scale bar, \* 1 mm, \*\* 10  $\mu$ m. P, proximal. D, distal. **b**, The distal nerve stump ATP levels with measured ROI ( $n=6$  mice per group). **c**, Representative images of toluidine blue staining, immunohistochemistry (NF-H/S-100B/DAPI), electron microscopy for each inhibitor in both sham and transection side. Scale bar, \* 10  $\mu$ m, \*\* 2  $\mu$ m. **d**, Quantification of the myelinated axon. **e-g**, Quantification of the G-ratio [e: cumulative G-ratio per individual; f, g: scatter plot, Spearman's rank correlation coefficient and  $p$  values showing G-ratio of individual myelinated axons against axon diameter ( $n=400$  in both (f) sham and (g) transection side) ( $n=4$  mice per group)]. **h**, Representative images of immunohistochemistry (MCT-1/S-100B/DAPI) for each inhibitor in both sham and transection side. Scale bar, \* 10  $\mu$ m. **i**, The number of MCT-1 positive Schwann cells ( $n=4$  mice per group). **j**, Representative images of mitochondrial findings for each inhibitor in both sham and transection side. Evaluation was performed in axons and Schwann cells separately. Scale bar, \* 200 nm. **k**, Violin plot of mitochondrial diameter (nm;  $n=200$ ). Cumulative mitochondria diameter per individual are also shown ( $n=4$  rat per group). **l**, Quantitative analysis of atypical mitochondria (%;  $n=4$  mice per group). All examinations were performed 1 d (24 h) after inhibitor administration and evaluated 3 mm distal from the sectional end and the corresponding uninjured nerve (Extended Data Fig. 7-1a). The concentrations of all inhibitors were determined from preliminarily experiments (Extended Data Fig. 7-1b-d), by measuring ATP levels 3 mm distal to the sectional end, with a 500  $\times$  500- $\mu$ m square (Extended Data Fig. 7-2). The ROI for measuring ATP levels was set at 3 mm distal from the sectional end, the center of the longitudinal nerve cross-section, with

*continued*

a  $300 \times 300\text{-}\mu\text{m}$  square (Extended Data Fig. 3-1). The OFF/GFP ratios ranged from 1.5 to 3.0. Immunohistochemistry showed the same results for the four individuals. A summary of the inhibition experiments is provided in Extended Data Table 7-1. Error bars indicate SD; \* $p < 0.05$ , \*\* $p < 0.01$ , \*\*\* $p < 0.001$ , two-way ANOVA followed by the Tukey's *post hoc* test (for comparison of sham group and transection group, respectively). No statistical data were available for mitochondrial diameter because there was no equal distribution. 2-DG, 2-deoxyglucose; 4-CIN, 4-cyano-4-hydroxycinnamic acid; MCT-1, monocarboxylate transporters 1; MSDC-0160, mitochondrial pyruvate carrier (MPC) inhibitors; ROI, region of interest.

ATP-related pathologic pathways involved at the distal nerve stump, have been variously reported (J. Wang et al., 2005; Di Stefano et al., 2014; Summers et al., 2014; Gerdts et al., 2015). Therefore, in this study, we used *GO-ATeam2* knock-in mouse and rat models, enabling the evaluation of ATP levels in the cytoplasm of axons and Schwann cells.

We showed that ATP levels 3 mm distal from the sectional end were maintained for 360 min and decreased 2 d later with fluorescence microscopy, and gradually decreased from 1 d later with two-photon microscopy. A previous *in vivo* study showed that the distal nerve stump ATP levels were maintained for over 30 h (Gerdts et al., 2015), this is almost consistent with our findings. However, an *in vitro* study without Schwann cells showed a rapid decrease in ATP levels (Yang et al., 2015). Our *in vivo* imaging with the *GO-ATeam2* probe demonstrated that the reaction of Schwann cells to energy retention after axotomy contributed to a gradual decrease in ATP levels. We also showed that ATP levels at the sectional end with fluorescence microscopy, decreased immediately after axotomy. This may be because of the initial physical damage with axotomy, since it takes a few hours for the initial response (Carvalho et al., 2019; Hussain et al., 2020). However, toluidine blue staining and electron microscopy revealed WD progression 2 d after axotomy, which was preceded by a decrease in ATP levels of the same lesion, measured by two-photon microscopy, 1 d after axotomy. The correlation between the WD and the ATP decreasing rate is consistent with that observed in previous reports (Beirowski et al., 2005; Yang et al., 2015).

In this study, we showed that the glycolytic system in both Schwann cells and axons is the primary metabolic source of ATP production in the distal nerve stump. Immunohistochemistry detected activation of glycolytic enzymes including HK-1, PFK-1, and LDHA in both Schwann cells and axons, and also detected a decrease in TCA cycle enzyme in axons. Mass spectrometry of the distal nerve stump revealed a decrease in ATP,  $\text{NAD}^+$ , and glycolytic intermediates including pyruvate. A previous study revealed that Schwann cells activated glycolysis to provide energy after axotomy by transporting glucose into cells via the glucose transporter 1 (GLUT1) and using glycolytic intermediates (Babetto et al., 2020). We additionally demonstrated the same metabolic changes in axons. The activation of LDHA in both Schwann cells and axons demonstrate the conversion of pyruvate to lactate and  $\text{NAD}^+$  (Doherty and Cleveland, 2013).  $\text{NAD}^+$  is crucial for the production of ATP in glycolysis (Fantin et al., 2006; Diaz-Garcia et al., 2017; Urbanska and Orzechowski, 2019; Osis et al., 2021). This is corroborated by the treatment of 2-DG in the transection side; compared with the

DMSO control group, the following was observed: WD progression and decreased levels of ATP without degenerated axonal mitochondria. These results suggested that the glycolytic system played an important role in maintaining ATP levels via  $\text{NAD}^+$  utilization that are generated from the catabolism with LDHA in the distal nerve stump in Schwann cells and axons.

We also found that MCTs in Schwann cells are activated after axotomy, which suggests its relevance in maintaining ATP levels in the distal nerve stump. An increase of MCT-1 positive Schwann cells was detected, using immunohistochemistry, after axotomy. Treatment with 4-CIN also demonstrated a remarkable progression of WD and decreased levels of ATP only in the transection side, and a slight progression of WD and unchanged levels of ATP in the sham side, compared with the DMSO group. Additionally, treatment with 2-DG, MSDC-0160, and 4-CIN demonstrated an increase in MCT-1 positive Schwann cells, compared with that observed in the DMSO group. In the PNS system, both MCT-1 and MCT-4 are expressed in Schwann cells (Garcia et al., 1994; Domènech-Estévez et al., 2015). In uninjured nerve, the absence of MCT-1 and MCT-4 in Schwann cells does not present developmental disorders of the PNS (Jha et al., 2020; Bouçanova et al., 2021). In contrast, in injured nerve, MCTs are activated to maintain axonal integrity by transporting monocarboxylate from Schwann cells to axons (Babetto et al., 2020). MCTs are also responsible for the passive and bidirectional transport of monocarboxylates such as pyruvate and lactate (Pérez-Escuredo et al., 2016). Given the need for pyruvate in axons, it is probable that pyruvate is transported from Schwann cells toward axons, whereas accumulated lactate in axons is transported from axons to Schwann cells. Additionally, lactate produced or transported by Schwann cells may be transported extracellularly via MCTs, which corroborates previous research that demonstrated extracellular lactate aggregation (Babetto et al., 2020). Our findings suggested that MCTs in Schwann cells are activated in cases of injury or energy metabolic inhibition, to support the activation of the glycolytic system in axons to efficiently maintain ATP levels.

We demonstrated that EP supplementation resulted in WD delay, increased numbers of MCT-1 positive Schwann cells, and elevated levels of ATP, compared with the saline group. In injured axons, EP supplementation delays WD by increasing ATP levels (J. Wang et al., 2005), inhibiting de-differentiation of Schwann cells through p-ERK1/2, p75NGFR, and lysosomal associated membrane protein 1 (Park et al., 2015), and preventing the expression of neuronal nitric oxide synthase (NOS1; Chung et al., 2019). Among these diverse pharmacological effects of EP, a constructive impact on ATP production was observed. Pyruvate delays WD by

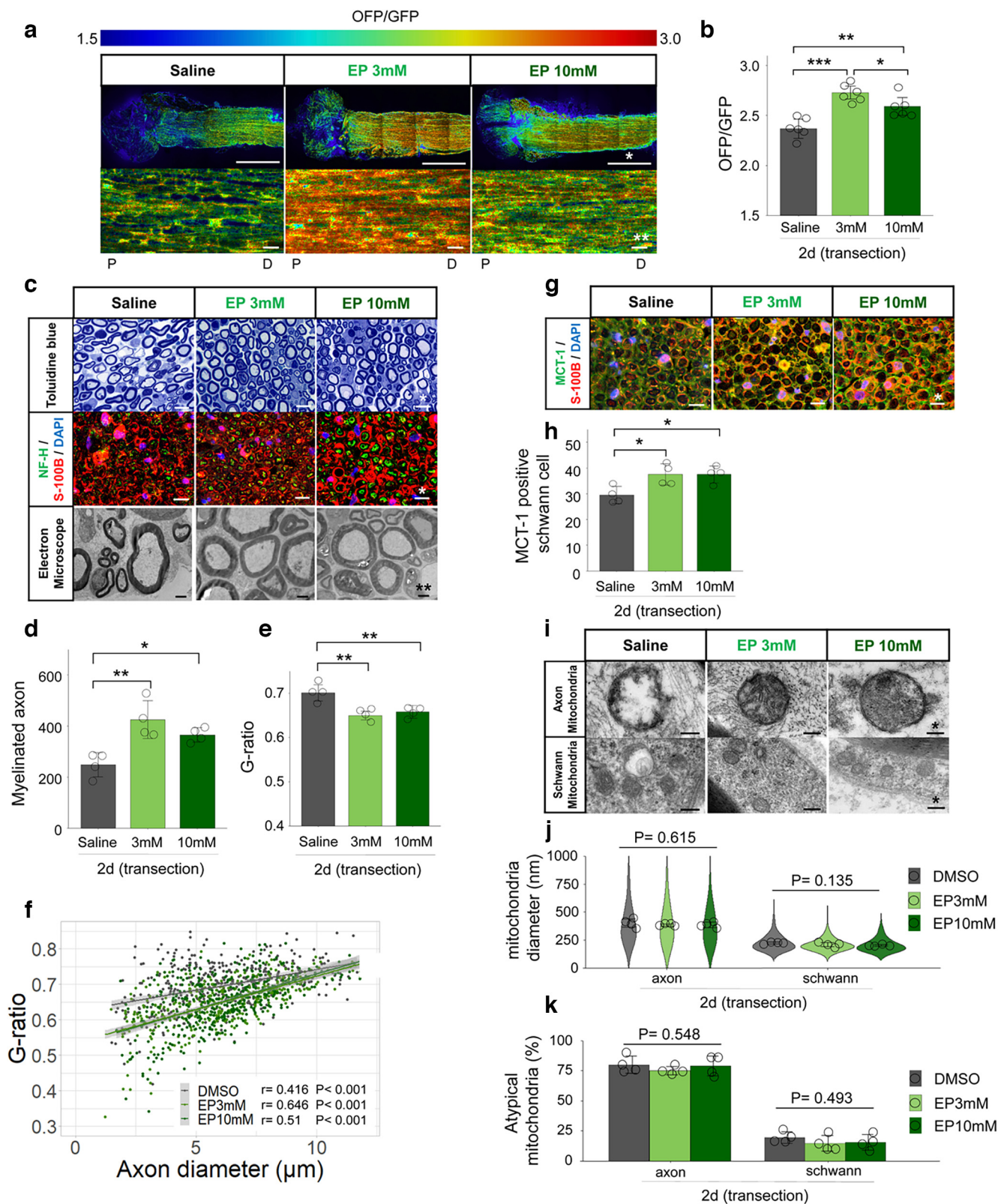


**Figure 8.** Ethyl pyruvate (EP) delays Wallerian degeneration with increased ATP levels. **a**, Representative ATP images for each treatment. Lower figures are enlarged image in the measured ROI. Upper figures present overall distal nerve stump image, from the sectional end. Scale bar, \* 1 mm, \*\* 10  $\mu$ m. P, proximal. D, distal. **b**, The distal nerve stump ATP levels with measured ROIs ( $n=6$  mice per group). **c**, Representative images of toluidine blue staining, immunohistochemistry (NF-H/S-100B/DAPI), electron microscopy, for each treatment. Scale bar, \* 10  $\mu$ m, \*\* 2  $\mu$ m. **d**, Quantification of the myelinated axon. **e**, **f**, Quantification of the G-ratio [e:

continued

cumulative G-ratio per individual, **f**: scatter plot, Spearman's rank correlation coefficient and *p* values showing G-ratio of individual myelinated axons against axon diameter ( $n = 400$ ) ( $n = 4$  mice per group). **g**, Representative images of immunohistochemistry (MCT-1/S-100B/DAPI) for each treatment. Scale bar, \*  $10\ \mu\text{m}$ . **h**, The number of MCT-1 positive Schwann cells ( $n = 4$  mice per group). **i**, Representative images of mitochondrial findings for each treatment. Evaluation was performed in axons and Schwann cells separately. Scale bar, \*  $200\ \text{nm}$ . **j**, Violin plot of mitochondrial diameter (nm;  $n = 200$ ). Cumulative mitochondria diameter per individual are also shown ( $n = 4$  rat per group). **k**, Quantitative analysis of atypical mitochondria (%;  $n = 4$  mice per group). All examinations were performed 2 d (48 h) after administration and evaluated 3 mm distal from the sectional end and the corresponding uninjured nerve. The ROI for measuring ATP levels was set at 3 mm distal from the sectional end, the center of the longitudinal nerve cross-section, with a  $300 \times 300\text{-}\mu\text{m}$  square (Extended Data Fig. 3-1). The OFP/GFP ratios ranged from 1.5 to 3.0. Immunohistochemistry showed the same results for the four individuals. Error bars indicate SD; \* $p < 0.05$ , \*\* $p < 0.01$ , \*\*\* $p < 0.001$ , one-way ANOVA followed by the Tukey's *post hoc* test (for comparison of sham group and transection group, respectively). EP, ethyl pyruvate; MCT-1, monocarboxylate transporters 1; ROI, region of interest.

inhibiting the activation of poly-ADP ribose polymerase 1 (PARP-1), which results in  $\text{NAD}^+$  depletion and inhibition of glycolysis (Zilberter et al., 2015). In addition, pyruvate contributes to ATP level maintenance through increased glycogen levels (Shetty et al., 2012). The results of EP supplementation experiment suggested that the additional pyruvate may have been transported from Schwann cells to axons via MCTs, thereby augmenting the glycolytic system and increasing ATP levels. EP supplementation concentrations have been reported to vary depending on the experimental system and route of administration (Park et al., 2015; Chung et al., 2019; Chavali et al., 2020; Gaikwad et al., 2021; Mao et al., 2021) thus EP toxicity at high concentrations (100 mM or higher) should be noted (Chung et al., 2019). In the present study, protective effects were observed in low concentrations (3 and 10 mM). The effects of high EP concentrations (30 and 100 mM) observed in this study indicates the toxicity inversely, thus it was desirable to identify the optimal dosage concentration of EP for the nervous system. Together, the present study suggested that to maintain ATP after axotomy, pyruvate is transported from Schwann cells to axons through MCTs, and both in Schwann cells and axons, pyruvate is metabolized by LDHA to generate  $\text{NAD}^+$  and promote metabolic shifts toward the glycolytic system, yet generate inadequate and inefficient ATP levels. We propose the model that the distal nerve stump produces ATP through MCT-induced monocarboxylate transport and the glycolytic system both in Schwann cells and axons (Fig. 9).

We also showed that TCA cycle in axons was not significantly associated with further progression of WD after axotomy. The treatment with MSDC-1060 of the transection side, demonstrated neither progression of WD nor decreased levels of ATP, compared with the DMSO group. In the distal nerve stump, previous studies also showed that mitochondrial disfunction model with carbonyl cyanide 3-chlorophenylhydrazone (CCCP) does not accelerate WD (Loreto et al., 2015). The protective effect of Wallerian degeneration slow (*wlds*) protein is independent of mitochondrial function (Kitay et al., 2013), and the contribution of mitochondrial dysfunction to WD progression has no established explanation (Merlini et al., 2022). Despite the inhibition of the glycolytic system, an upstream metabolic pathway to the TCA cycle, 2-DG demonstrated no change of axonal mitochondrial atypicality in the transection side compared with DMSO group. These findings suggest that the TCA cycle may be not significantly

associated with the salvage pathway during WD, as a metabolic source of ATP.

Although this study demonstrated biochemical alterations after axotomy, the TCA cycle can also be considered an essential energy metabolic pathway for efficient ATP production. First, in the distal nerve stump, we demonstrated ~80% axonal mitochondrial atypicality, decreased levels of ATP, and decreased availability of the TCA cycle intermediates and enzymes. That is, ~20% of the mitochondria in axons are maintained 2 d after axotomy. It was previously reported that calcium overload caused an opening of the mitochondrial permeability transition pore (mPTP) and a decrease in mitochondrial ATP, which lead to WD progression in the distal nerve stump (Villegas et al., 2014). It was also reported that mitochondrial localization of NMNAT activity results in increased ATP synthetic capacity without affecting the expression of the mitochondrial enzymes profile of the respiratory chain (Yahata et al., 2009), and increased NMNAT activity delayed WD (Araki et al., 2004). These findings indicated that the inactivation of TCA cycle is associated with gradually decreased levels of ATP after 1 or 2 d after axotomy, and also suggested that activation of TCA cycle through NMNAT activity may delay WD. The production of ATP by the TCA cycle is not fully inactivated after axotomy and may still persist to a certain degree. Second, we showed that the treatment with MSDC-1060 of the sham side, demonstrated decreased levels of ATP and progression of WD, compared with the DMSO group. The TCA cycle functions in the mitochondrial matrix and requires the influx of pyruvate via the MPC1 and MPC2 to initiate the reaction (Bricker et al., 2012), and the defect of MPC disrupts the homeostasis of glucose metabolism (Sébastien Herzig, 2012; Vigueira et al., 2014). In uninjured axons, mitochondrial dysfunction is associated with WD in uninjured axons; CCCP triggers mitochondrial depolarization and leads to WD (Loreto et al., 2020). Together, these findings suggested that the TCA cycle is responsible for maintaining uninjured nerve stability and its ATP levels, and also may be partially responsible for injured nerve. Further investigations are necessary to elucidate the correlation between the TCA cycle and the ATP-related salvage pathway during WD.

A recent study showed the necessity of the glycolytic system in axons for not only axonal maintenance but also regeneration (Ketschek et al., 2021). The current study focuses on the novel perspective of the glycolytic system rather than mitochondrial function, which has been attracted



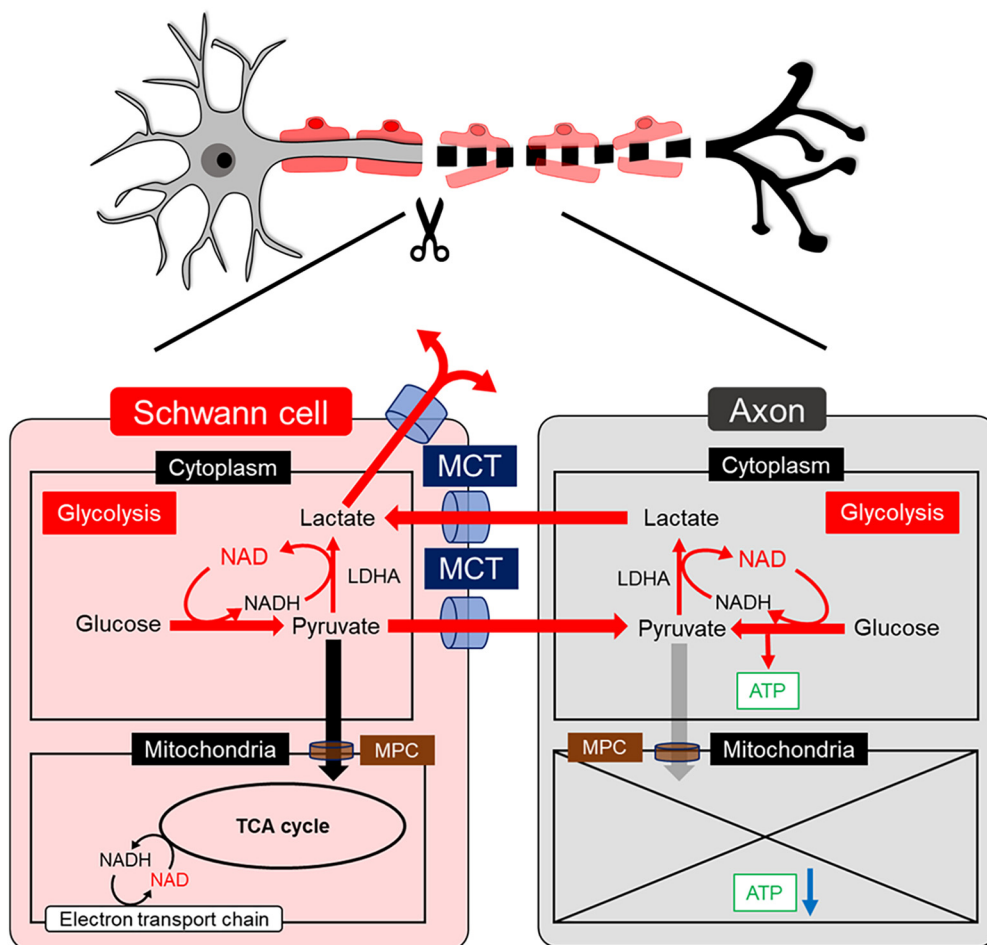


**Figure 9.** Model depicting changes in the energy metabolism of Schwann cells and axons after axotomy. The proposed metabolic changes in the distal nerve stump. In Schwann cells, the glycolytic system and MCT-induced monocarboxylate transport are activated. In axons, the glycolytic system is activated, whereas TCA cycle is inactivated because of mitochondrial degeneration. The glycolytic intermediate, pyruvate is transported from Schwann cells to axons through MCTs, and both in Schwann cells and axons, pyruvate is metabolized by LDHA to generate  $\text{NAD}^+$  and promote metabolic shifts toward the glycolytic system to produce ATP. The main metabolic source of ATP is mainly on glycolytic system both in Schwann cells and axons. The excess produced lactate in axons is transported to Schwann cells, subsequently released to extracellular space via MCTs.

significant attention in neuronal metabolism (Sheng, 2017). The axons initiated axonal regeneration without migrating Schwann cells in the acute phase, within 5 d of axotomy, which occurred concurrently with WD progression (Min et al., 2021). Glycolytic intermediates support cells involved in axon regeneration, such as macrophages, mesenchymal and endothelial cells (Cattin et al., 2015; Babetto and Beirowski, 2022). Therefore, the activation of the glycolytic system in axons may be a strongly associated with WD delay and axon regeneration. Axonal regeneration and prevention of muscle atrophy following the early neurotrophin (Yuan et al., 2019; Raza et al., 2020), may be supported by axonal ATP retention. Additional studies would be needed to clarify the mechanisms of neuronal metabolism with focusing on the glycolytic system.

There are some limitations in this study. First, the local administration experiments of inhibitors and pyruvate were targeted in both Schwann cells and axons. ATP levels were also targeted at the center of the longitudinal

nerve cross-section even in two-photon microscopy imaging. The Schwann cells and axons could not be completely separated. In addition, Schwann cells make up ~45–70% of the cellular components in the peripheral nerve (Stierli et al., 2018; Yim et al., 2022), and interference with ATP levels by macrophages and other constituent cells such as endoneurial fibroblasts, adipocytes, and pericytes, should be considered (Stierli et al., 2018; Stassart and Woodhoo, 2020; Yim et al., 2022). These problems would be solved by using Schwann cell-specific ( $\text{P0-Cre}$ ) and axon-specific ( $\text{NFH-Cre}$ )  $\text{GO-ATeam2}$  knock-in mice (Feltri et al., 1999; Scemes et al., 2019). Alternatively, we showed the activation of the glycolytic system and TCA cycle in Schwann cells and in axons by immunohistochemistry. Second, the present study did not thoroughly analyze the role of the TCA cycle in the progression of WD. Previous studies suggested that the TCA cycle is associated with active processes in WD. The TCA cycle produces ATP via autophagic activity (Lum et al., 2005). Autophagy is triggered

by glycogen synthase kinase 3B (GSK3B)-induced activation of mitochondrial MCL1, and contributes to local ATP in degenerating axons, which is required for normal recruitment of phagocytes to axonal debris *in vivo* (Wakatsuki et al., 2017). In this study, only infiltrated CD68 macrophages were detected after axotomy, and its metabolic interaction was not investigated. We should note that the TCA cycle is also involved in the ATP-related auto-destruction programs during WD, as well as in the salvage pathway. Furthermore, the treatment with MSDC-0160 in the transection side did not demonstrate decreased levels of ATP or progression of WD as compared with the DMSO group. The adjuvant effect of pharmacological treatment may be relatively modest considering the spontaneous axonal mitochondrial degeneration in the distal nerve stumps. Finally, the potential effects of MCTs on Schwann cells remain unclear (Jha et al., 2020). Cell-specific experimental methods are required to support the results reported herein.

Our study expanded the understanding of spatiotemporal ATP levels in injured peripheral nerve and the dynamics of energy metabolism in WD. Our findings suggest a metabolic shift toward the glycolytic system for maintaining ATP levels, both in Schwann cells and in axons. This study provides a basis for understanding the bioenergetics during WD, and could be used in the development of therapeutic agents.

## References

- Adalbert R, Gillingwater TH, Haley JE, Bridge K, Beirowski B, Berek L, Wagner D, Grumme D, Thomson D, Celik A, Addicks K, Ribchester RR, Coleman MP (2005) A rat model of slow Wallerian degeneration (WdS) with improved preservation of neuromuscular synapses. *Eur J Neurosci* 21:271–277.
- Alvarez-Prats A, Bjelobaba I, Aldworth Z, Baba T, Abebe D, Kim YJ, Stojilkovic SS, Stopfer M, Balla T (2018) Schwann-cell-specific deletion of phosphatidylinositol 4-kinase alpha causes aberrant myelination. *Cell Rep* 23:2881–2890.
- Anamitra Ghosh TT, George S, Hildebrandt EN, Steiner JA, Madaj Z, Schulz E, Machiela E, McDonald WG, Escobar Galvis ML, Kordower JH, Van Raamsdonk JM, Colca JR, Brundin P (2016) Mitochondrial pyruvate carrier regulates autophagy, inflammation, and neurodegeneration in experimental models of Parkinson's disease. *Sci Transl Med* 8:368ra174.
- Araki T, Sasaki Y, Milbrandt J (2004) Increased nuclear NAD biosynthesis and SIRT1 activation prevent axonal degeneration. *Science* 305:1010–1013.
- Babetto E, Beirowski B (2022) Stressed axons craving for glial sugar: links to regeneration? *Neural Regen Res* 17:304–306.
- Babetto E, Beirowski B, Russler EV, Milbrandt J, DiAntonio A (2013) The Phr1 ubiquitin ligase promotes injury-induced axon self-destruction. *Cell Rep* 3:1422–1429.
- Babetto E, Wong KM, Beirowski B (2020) A glycolytic shift in Schwann cells supports injured axons. *Nat Neurosci* 23:1215–1228.
- Barrientos SA, Martinez NW, Yoo S, Jara JS, Zamorano S, Hetz C, Twiss JL, Alvarez J, Court FA (2011) Axonal degeneration is mediated by the mitochondrial permeability transition pore. *J Neurosci* 31:966–978.
- Beirowski B, Adalbert R, Wagner D, Grumme DS, Addicks K, Ribchester RR, Coleman MP (2005) The progressive nature of Wallerian degeneration in wild-type and slow Wallerian degeneration (WdS) nerves. *BMC Neurosci* 6:6.
- Beirowski B, Nográdi A, Babetto E, Garcia-Alias G, Coleman MP (2010) Mechanisms of axonal spheroid formation in central nervous system Wallerian degeneration. *J Neuropathol Exp Neurol* 69:455–472.
- Beirowski B, Babetto E, Golden JP, Chen YJ, Yang K, Gross RW, Patti GJ, Milbrandt J (2014) Metabolic regulator LKB1 is crucial for Schwann cell-mediated axon maintenance. *Nat Neurosci* 17:1351–1361.
- Beirowski B, Wong KM, Babetto E, Milbrandt J (2017) mTORC1 promotes proliferation of immature Schwann cells and myelin growth of differentiated Schwann cells. *Proc Natl Acad Sci USA* 114:E4261–E4270.
- Bouçanova F, Chrast R (2020) Metabolic interaction between Schwann cells and axons under physiological and disease conditions. *Front Cell Neurosci* 14:148.
- Bouçanova F, Pollmeier G, Sandor K, Morado Urbina C, Nijssen J, Médard JJ, Bartesaghi L, Pellerin L, Svensson CI, Hedlund E, Chrast R (2021) Disrupted function of lactate transporter MCT1, but not MCT4, in Schwann cells affects the maintenance of motor end-plate innervation. *Glia* 69:124–136.
- Bricker DK, Taylor EB, Schell JC, Orsak T, Boutron A, Chen YC, Cox JE, Cardon CM, Van Vranken JG, Dephoure N, Redin C, Boudina S, Gygi SP, Brivet M, Thummel CS, Rutter J (2012) A mitochondrial pyruvate carrier required for pyruvate uptake in yeast, *Drosophila*, and humans. *Science* 337:96–100.
- Carvalho CR, Oliveira JM, Reis RL (2019) Modern trends for peripheral nerve repair and regeneration: beyond the hollow nerve guidance conduit. *Front Bioeng Biotechnol* 7:337.
- Cattin AL, Burden JJ, Van Emmenis L, Mackenzie FE, Hoving JJ, Garcia Calavia N, Guo Y, McLaughlin M, Rosenberg LH, Quereda V, Jamecna D, Napoli I, Parrinello S, Enver T, Ruhrberg C, Lloyd AC (2015) Macrophage-induced blood vessels guide Schwann cell-mediated regeneration of peripheral nerves. *Cell* 162:1127–1139.
- Chavali VD, Agarwal M, Vyas VK, Saxena B (2020) Neuroprotective effects of ethyl pyruvate against aluminum chloride-induced Alzheimer's disease in rats via inhibiting toll-like receptor 4. *J Mol Neurosci* 70:836–850.
- Chen YF, Chen LH, Yeh YM, Wu PY, Chen YF, Chang LY, Chang JY, Shen MR (2017) Minoxidil is a potential neuroprotective drug for paclitaxel-induced peripheral neuropathy. *Sci Rep* 7:45366.
- Chung HJ, Kim M, Jung J, Jeong NY (2019) Inhibition of neuronal nitric oxide synthase by ethyl pyruvate in Schwann cells protects against peripheral nerve degeneration. *Neurochem Res* 44:1964–1976.
- Coleman MP, Höke A (2020) Programmed axon degeneration: from mouse to mechanism to medicine. *Nat Rev Neurosci* 21:183–196.
- Conforti L, Gilley J, Coleman MP (2014) Wallerian degeneration: an emerging axon death pathway linking injury and disease. *Nat Rev Neurosci* 15:394–409.
- Cong L, Ran FA, Cox D, Lin S, Barretto R, Habib N, Hsu PD, Wu X, Jiang W, Marraffini LA, Zhang F (2013) Multiplex genome engineering using CRISPR/Cas systems. *Science* 339:819–823.
- Di Stefano M, et al. (2014) A rise in NAD precursor nicotinamide mononucleotide (NMN) after injury promotes axon degeneration. *Cell Death Differ* 22:731–742.
- Diaz-Garcia CM, Mongeon R, Lahmann C, Koveal D, Zucker H, Yellen G (2017) Neuronal stimulation triggers neuronal glycolysis and not lactate uptake. *Cell Metab* 26:361–374.e4.
- Doherty JR, Cleveland JL (2013) Targeting lactate metabolism for cancer therapeutics. *J Clin Invest* 123:3685–3692.
- Domènech-Estévez E, Baloui H, Repond C, Rosafio K, Médard JJ, Tricaud N, Pellerin L, Chrast R (2015) Distribution of monocarboxylate transporters in the peripheral nervous system suggests putative roles in lactate shuttling and myelination. *J Neurosci* 35:4151–4156.
- Fantin VR, St-Pierre J, Leder P (2006) Attenuation of LDH-A expression uncovers a link between glycolysis, mitochondrial physiology, and tumor maintenance. *Cancer Cell* 9:425–434.
- Feltri ML, D'Antonio M, Previtali S, Fasolini M, Messing A, Wrabetz L (1999) PO-Cre transgenic mice for inactivation of adhesion molecules in Schwann cells. *Ann N Y Acad Sci* 883:116–123.

- Gaikwad S, Puangmalai N, Bittar A, Montalbano M, Garcia S, McAllen S, Bhatt N, Sonawane M, Sengupta U, Kaye R (2021) Tau oligomer induced HMGB1 release contributes to cellular senescence and neuropathology linked to Alzheimer's disease and frontotemporal dementia. *Cell Rep* 36:109419.
- Garcia CK, Goldstein JL, Pathak RK, Anderson RG, Brown MS (1994) Molecular characterization of a membrane transporter for lactate, pyruvate, and other monocarboxylates: implications for the Cori cycle. *Cell* 76:865–873.
- Gerdts J, Brace EJ, Sasaki Y, DiAntonio A, Milbrandt J (2015) SARM1 activation triggers axon degeneration locally via NAD(+) destruction. *Science* 348:453–457.
- Gerdts J, Summers DW, Milbrandt J, DiAntonio A (2016) Axon self-destruction: new links among SARM1, MAPKs, and NAD+ metabolism. *Neuron* 89:449–460.
- Gilley J, Coleman MP (2010) Endogenous Nmnat2 is an essential survival factor for maintenance of healthy axons. *PLoS Biol* 8:e1000300.
- Halestrap AP (2012) The mitochondrial pyruvate carrier: has it been unearthed at last? *Cell Metab* 16:141–143.
- Han SM, Baig HS, Hammarlund M (2016) Mitochondria localize to injured axons to support regeneration. *Neuron* 92:1308–1323.
- Haris M, Singh A, Cai K, Kogan F, McGarvey J, Debrosse C, Zsido GA, Witschey WR, Koomalsingh K, Pilla JJ, Chirinos JA, Ferrari VA, Gorman JH, Hariharan H, Gorman RC, Reddy R (2014) A technique for in vivo mapping of myocardial creatine kinase metabolism. *Nat Med* 20:209–214.
- Hussain G, Wang J, Rasul A, Anwar H, Qasim M, Zafar S, Aziz N, Razzaq A, Hussain R, de Aguiar JG, Sun T (2020) Current status of therapeutic approaches against peripheral nerve injuries: a detailed story from injury to recovery. *Int J Biol Sci* 16:116–134.
- Ichihara Y, Doi T, Ryu Y, Nagao M, Sawada Y, Ogata T (2017) Oligodendrocyte progenitor cells directly utilize lactate for promoting cell cycling and differentiation. *J Cell Physiol* 232:986–995.
- Jha MK, Lee Y, Russell KA, Yang F, Dastgheyb RM, Deme P, Ament XH, Chen W, Liu Y, Guan Y, Polydefkis MJ, Hoke A, Haughey NJ, Rothstein JD, Morrison BM (2020) Monocarboxylate transporter 1 in Schwann cells contributes to maintenance of sensory nerve myelination during aging. *Glia* 68:161–177.
- Jia L, Liao M, Mou A, Zheng Q, Yang W, Yu Z, Cui Y, Xia X, Qin Y, Chen M, Xiao B (2021) Rheb-regulated mitochondrial pyruvate metabolism of Schwann cells linked to axon stability. *Dev Cell* 56:1–15.
- Kennedy HJ, Pouli AE, Ainscow EK, Jouaville LS, Rizzuto R, Rutter GA (1999) Glucose generates sub-plasma membrane ATP microdomains in single islet beta-cells. Potential role for strategically located mitochondria. *J Biol Chem* 274:13281–13291.
- Ketschek A, Sainath R, Holland S, Gallo G (2021) The axonal glycolytic pathway contributes to sensory axon extension and growth cone dynamics. *J Neurosci* 41:6637–6651.
- Kitay BM, McCormack R, Wang Y, Tsoulfas P, Zhai RG (2013) Mislocalization of neuronal mitochondria reveals regulation of Wallerian degeneration and NMNAT/WLD(S)-mediated axon protection independent of axonal mitochondria. *Hum Mol Genet* 22:1601–1614.
- Lau C, Niere M, Ziegler M (2009) The NMN/NaMN adenyllyltransferase (NMNAT) protein family. *Front Biosci (Landmark Ed)* 14:410–431.
- Lenzi P, Marongiu R, Falleni A, Gelmetti V, Busceti CL, Michiorri S, Valente EM, Fornai F (2012) A subcellular analysis of genetic modulation of PINK1 on mitochondrial alterations, autophagy and cell death. *Arch Ital Biol* 150:194–217.
- Li F, Sami A, Noristani HN, Slattery K, Qiu J, Groves T, Wang S, Veerasammy K, Chen YX, Morales J, Haynes P, Sehgal A, He Y, Li S, Song Y (2020) Glial metabolic rewiring promotes axon regeneration and functional recovery in the central nervous system. *Cell Metab* 32:767–785.e7.
- Loreto A, Di Stefano M, Gering M, Conforti L (2015) Wallerian degeneration is executed by an NMN-SARM1-dependent late Ca(2+) influx but only modestly influenced by mitochondria. *Cell Rep* 13:2539–2552.
- Loreto A, Hill CS, Hewitt VL, Orsomando G, Angeletti C, Gilley J, Lucci C, Sanchez-Martinez A, Whitworth AJ, Conforti L, Dajas-Bailador F, Coleman MP (2020) Mitochondrial impairment activates the Wallerian pathway through depletion of NMNAT2 leading to SARM1-dependent axon degeneration. *Neurobiol Dis* 134:104678.
- Lum JJ, DeBerardinis RJ, Thompson CB (2005) Autophagy in metazoans: cell survival in the land of plenty. *Nat Rev Mol Cell Biol* 6:439–448.
- Mao L, Sun L, Sun J, Sun B, Gao Y, Shi H (2021) Ethyl pyruvate improves white matter remodeling in rats after traumatic brain injury. *CNS Neurosci Ther* 27:113–122.
- Merlini E, Coleman MP, Loreto A (2022) Mitochondrial dysfunction as a trigger of programmed axon death. *Trends Neurosci* 45:53–63.
- Min Q, Parkinson DB, Dun XP (2021) Migrating Schwann cells direct axon regeneration within the peripheral nerve bridge. *Glia* 69:235–254.
- Miranda-Goncalves V, Honavar M, Pinheiro C, Martinho O, Pires MM, Pinheiro C, Cordeiro M, Bebiano G, Costa P, Palmeirim I, Reis RM, Baltazar F (2013) Monocarboxylate transporters (MCTs) in gliomas: expression and exploitation as therapeutic targets. *Neuro Oncol* 15:172–188.
- Misgeld T, Kerschensteiner M, Bareyre FM, Burgess RW, Lichtman JW (2007) Imaging axonal transport of mitochondria in vivo. *Nat Methods* 4:559–561.
- Morikawa T, Kajimura M, Nakamura T, Hishiki T, Nakanishi T, Yukutake Y, Nagahata Y, Ishikawa M, Hattori K, Takenouchi T, Takahashi T, Ishii I, Matsubara K, Kabe Y, Uchiyama S, Nagata E, Gadalla MM, Snyder SH, Suematsu M (2012) Hypoxic regulation of the cerebral microcirculation is mediated by a carbon monoxide-sensitive hydrogen sulfide pathway. *Proc Natl Acad Sci USA* 109:1293–1298.
- Nakajima N, Ohnishi Y, Yamamoto M, Setoyama D, Imai H, Takenaka T, Matsumoto M, Hosomi K, Saitoh Y, Furue H, Kishima H (2022) Excess intracellular ATP causes neuropathic pain following spinal cord injury. *Cell Mol Life Sci* 79:483.
- Nakano M, Imamura H, Nagai T, Noji H (2011) Ca(2+)-regulation of mitochondrial ATP synthesis visualized at the single cell level. *ACS Chem Biol* 6:709–715.
- Natale G, Lenzi P, Lazzeri G, Falleni A, Biagioni F, Ryskalin L, Fornai F (2015) Compartment-dependent mitochondrial alterations in experimental ALS, the effects of mitophagy and mitochondrial biogenesis. *Front Cell Neurosci* 9:434.
- Nixon RA (2013) The role of autophagy in neurodegenerative disease. *Nat Med* 19:983–997.
- Nocera G, Jacob C (2020) Mechanisms of Schwann cell plasticity involved in peripheral nerve repair after injury. *Cell Mol Life Sci* 77:3977–3989.
- Ohnishi Y, Yamamoto M, Sugiura Y, Setoyama D, Kishima H (2021) Rostro-caudal different energy metabolism leading to differences in degeneration in spinal cord injury. *Brain Commun* 3:fcab058.
- Osis G, Traylor AM, Black LM, Spangler D, George JF, Zarjou A, Verlander JW, Agarwal A (2021) Expression of lactate dehydrogenase A and B isoforms in the mouse kidney. *Am J Physiol Renal Physiol* 320:F706–F718.
- Park BS, Jo HW, Park C, Huh Y, Jung J, Jeong NY (2015) A novel effect of ethyl pyruvate in Schwann cell de-differentiation and proliferation during Wallerian degeneration. *Anim Cells Syst* 19:262–268.
- Patterson JN, Cousteils K, Lou JW, Manning Fox JE, MacDonald PE, Joseph JW (2014) Mitochondrial metabolism of pyruvate is essential for regulating glucose-stimulated insulin secretion. *J Biol Chem* 289:13335–13346.
- Pérez-Escuredo J, Van Hée VF, Sboarina M, Falces J, Payen VL, Pellerin L, Sonveaux P (2016) Monocarboxylate transporters in the brain and in cancer. *Biochim Biophys Acta* 1863:2481–2497.
- Pivovarova NB, Andrews SB (2010) Calcium-dependent mitochondrial function and dysfunction in neurons. *FEBS J* 277:3622–3636.

- Press C, Milbrandt J (2008) Nmnat delays axonal degeneration caused by mitochondrial and oxidative stress. *J Neurosci* 28:4861–4871.
- Raza C, Riaz HA, Anjum R, Shakeel NUA (2020) Repair strategies for injured peripheral nerve: review. *Life Sci* 243:117308.
- Roberts SL, Dun XP, Doddrell RDS, Mindos T, Drake LK, Onaitis MW, Florio F, Quattrini A, Lloyd AC, D'Antonio M, Parkinson DB (2017) Sox2 expression in Schwann cells inhibits myelination in vivo and induces influx of macrophages to the nerve. *Development* 144:3114–3125.
- Sasaki Y, Hackett AR, Kim S, Strickland A, Milbrandt J (2018) Dysregulation of NAD(+) metabolism induces a Schwann cell differentiation program. *J Neurosci* 38:6546–6562.
- Savastano LE, Laurito SR, Fitt MR, Rasmussen JA, Gonzalez Polo V, Patterson SI (2014) Sciatic nerve injury: a simple and subtle model for investigating many aspects of nervous system damage and recovery. *J Neurosci Methods* 227:166–180.
- Scemes E, Velišek L, Velišková J (2019) Astrocyte and neuronal Pannexin1 contribute distinctly to seizures. *ASN Neuro* 11:1759091419833502.
- Sébastien Herzig ER, Montessuit S, Veuthey J-L, Zamboni N, Westermann B, Kunji ERS, Martinou J-C (2012) Identification and functional expression of the mitochondrial pyruvate carrier. *Science* 337:93–96.
- Sheng ZH (2017) The interplay of axonal energy homeostasis and mitochondrial trafficking and anchoring. *Trends Cell Biol* 27:403–416.
- Shetty PK, Sadgrove MP, Galeffi F, Turner DA (2012) Pyruvate incubation enhances glycogen stores and sustains neuronal function during subsequent glucose deprivation. *Neurobiol Dis* 45:177–187.
- Stassart RM, Woodhoo A (2020) Axo-glia interaction in the injured PNS. *Dev Neurobiol* 81:490–506.
- Stierli S, Napoli I, White IJ, Cattin AL, Monteza Cabrejos A, Garcia Calavia N, Malong L, Ribeiro S, Nihouarn J, Williams R, Young KM, Richardson WD, Lloyd AC (2018) The regulation of the homeostasis and regeneration of peripheral nerve is distinct from the CNS and independent of a stem cell population. *Development* 145:dev170316.
- Summers DW, DiAntonio A, Milbrandt J (2014) Mitochondrial dysfunction induces Sarm1-dependent cell death in sensory neurons. *J Neurosci* 34:9338–9350.
- Trimarco A, Taveggia C (2020) Schwann cell energy to die for. *Nat Neurosci* 23:1179–1181.
- Tsuyama T, Kishikawa J, Han YW, Harada Y, Tsubouchi A, Noji H, Kakizuka A, Yokoyama K, Uemura T, Imamura H (2013) In vivo fluorescent adenosine 5'-triphosphate (ATP) imaging of *Drosophila melanogaster* and *Caenorhabditis elegans* by using a genetically encoded fluorescent ATP biosensor optimized for low temperatures. *Anal Chem* 85:7889–7896.
- Urbanska K, Orzechowski A (2019) Unappreciated role of LDHA and LDHB to control apoptosis and autophagy in tumor cells. *Int J Mol Sci* 20:2085.
- Vargas ME, Barres BA (2007) Why is Wallerian degeneration in the CNS so slow? *Annu Rev Neurosci* 30:153–179.
- Viader A, Sasaki Y, Kim S, Strickland A, Workman CS, Yang K, Gross RW, Milbrandt J (2013) Aberrant Schwann cell lipid metabolism linked to mitochondrial deficits leads to axon degeneration and neuropathy. *Neuron* 77:886–898.
- Vigueira PA, McCommis KS, Schweitzer GG, Remedi MS, Chambers KT, Fu X, McDonald WG, Cole SL, Colca JR, Kletzien RF, Burgess SC, Finck BN (2014) Mitochondrial pyruvate carrier 2 hypomorphism in mice leads to defects in glucose-stimulated insulin secretion. *Cell Rep* 7:2042–2053.
- Villegas R, Martinez NW, Lillo J, Pihan P, Hernandez D, Twiss JL, Court FA (2014) Calcium release from intra-axonal endoplasmic reticulum leads to axon degeneration through mitochondrial dysfunction. *J Neurosci* 34:7179–7189.
- Wakatsuki S, Tokunaga S, Shibata M, Araki T (2017) GSK3B-mediated phosphorylation of MCL1 regulates axonal autophagy to promote Wallerian degeneration. *J Cell Biol* 216:477–493.
- Waller A (1851) Experiments on the section of the glosso-pharyngeal and hypoglossal nerves of the frog, and observations of the alterations produced thereby in the structure of their primitive fibres. *Edinb Med Surg J* 76:369–376.
- Wang B, Huang M, Shang D, Yan X, Zhao B, Zhang X (2021) Mitochondrial behavior in axon degeneration and regeneration. *Front Aging Neurosci* 13:650038.
- Wang J, Zhai Q, Chen Y, Lin E, Gu W, McBurney MW, He Z (2005) A local mechanism mediates NAD-dependent protection of axon degeneration. *J Cell Biol* 170:349–355.
- Wang J, Hamm RJ, Povlishock JT (2011) Traumatic axonal injury in the optic nerve: evidence for axonal swelling, disconnection, die-back, and reorganization. *J Neurotrauma* 28:1185–1198.
- Wang JT, Medress ZA, Barres BA (2012) Axon degeneration: molecular mechanisms of a self-destruction pathway. *J Cell Biol* 196:7–18.
- Yagi HKN, Tanaka H, Tsukihara T, Kato-Yamada Y, Yoshida M, Akutsu H (2007) Structures of the thermophilic F1-ATPase epsilon subunit suggesting ATP-regulated arm motion of its C-terminal domain in F1. *Proc Natl Acad Sci USA* 104:11233–11238.
- Yahata N, Yuasa S, Araki T (2009) Nicotinamide mononucleotide adenyltransferase expression in mitochondrial matrix delays Wallerian degeneration. *J Neurosci* 29:6276–6284.
- Yamamoto M, Kim M, Imai H, Itakura Y, Ohtsuki G (2019) Microglia-triggered plasticity of intrinsic excitability modulates psychomotor behaviors in acute cerebellar inflammation. *Cell Rep* 28:2923–2938 e2928.
- Yang J, Wu Z, Renier N, Simon DJ, Uryu K, Park DS, Greer PA, Tournier C, Davis RJ, Tessier-Lavigne M (2015) Pathological axonal death through a MAPK cascade that triggers a local energy deficit. *Cell* 160:161–176.
- Yim AKY, Wang PL, Birmingham JR Jr, Hackett A, Strickland A, Miller TM, Ly C, Mitra RD, Milbrandt J (2022) Disentangling glial diversity in peripheral nerves at single-nuclei resolution. *Nat Neurosci* 25:238–251.
- Yuan YS, Niu SP, Yu YL, Zhang PX, Yin XF, Han N, Zhang YJ, Zhang DY, Xu HL, Kou YH, Jiang BG (2019) Reinnervation of spinal cord anterior horn cells after median nerve repair using transposition with other nerves. *Neural Regen Res* 14:699–705.
- Zhou B, Yu P, Lin MY, Sun T, Chen Y, Sheng ZH (2016) Facilitation of axon regeneration by enhancing mitochondrial transport and rescuing energy deficits. *J Cell Biol* 214:103–119.
- Zilberter Y, Gubkina O, Ivanov AI (2015) A unique array of neuroprotective effects of pyruvate in neuropathology. *Front Neurosci* 9:17.